


Boundary-layer modeling of polymer-based acoustofluidic devices

Sazid Z. Hoque^{✉*} and Henrik Bruus^{✉†}

Department of Physics, *Technical University of Denmark*, DTU Physics Building 309, DK-2800 Kongens Lyngby, Denmark

 (Received 7 July 2025; revised 30 September 2025; accepted 2 October 2025; published 30 October 2025)

In fluid-filled microchannels embedded in solid devices and driven by megahertz ultrasound transducers, the thickness of the viscous boundary layer in the fluid near the confining walls is typically three to four orders of magnitude smaller than the acoustic wavelength and five orders of magnitude smaller than the longest dimension of the device. This large span in length scale renders direct numerical simulations of such devices prohibitively expensive in terms of computer memory requirements, and consequently the so-called boundary-layer models are introduced. In such models, approximate analytical expressions of the boundary-layer fields are found and inserted in the governing equations and boundary conditions for the remaining bulk fields. Since the bulk fields do not vary across the boundary layers, they can be computed numerically using the resulting boundary-layer model without resolving the boundary layers. However, current boundary-layer models are only accurate for hard solids (e.g., glass and silicon) with relatively small oscillation amplitudes of the confining wall, and they fail for soft solids (e.g., polymers) with larger wall oscillations. In this work, we extend the boundary-layer model of Bach and Bruus, *J. Acoust. Soc. Am.* **144**, 766 (2018) to enable accurate simulation of soft-walled devices. The extended model is validated by comparison (1) with direct numerical simulations in three and two dimensions of tiny submillimeter- and larger millimeter-sized polymer devices, respectively, and (2) with previously published experimental data.

DOI: [10.1103/m1rf-tkpw](https://doi.org/10.1103/m1rf-tkpw)

I. INTRODUCTION

Acoustofluidic devices based on bulk acoustic waves show promising applications in contactless manipulation of micro-objects [1,2], such as separation of bacteria from blood lysate [3], cancer cells enrichment in blood [4,5], optimized microparticle focusing [6,7], and other cell manipulations [8]. These devices are also used for manipulation of immiscible fluid interfaces [9,10] and inhomogeneous fluids [11–14].

Traditionally, bulk-acoustic-wave devices are fabricated using hard materials with high Q factors, such as glass and silicon [15]. Although such devices can be manufactured with high accuracy and throughput, the fabrication process may be expensive, limiting in particular their single-use applications. Alternatively, polymer-based devices can be used, which is advantageous for bulk production at minimal cost compared to glass-silicon devices [16–20].

However, it is difficult to establish the acoustic fields in a polymer system due to the low acoustic contrast between the polymer and the fluid.

Recently, the formation of pressure nodal planes in polymer systems has been elucidated by Moiseyenko and Bruus [21] by introducing the principle of whole-system ultrasound resonances (WSURs). According to this principle, acoustic resonances in polymer devices are determined by the dimensions of the whole system, and by the acoustic contrast between the ambient air and the system. Among the obtained WSUR modes, the ones leading to a robust acoustic response inside the fluid cavity are selected. Successful focusing of particles in polymer-based acoustofluidic devices designed using the WSUR principle has been demonstrated by experiments and simulations [20].

Despite the significant advancement in numerical modeling of acoustofluidic devices in the past decade [22–26], it remains a challenge to have a robust, computationally efficient method that captures all the relevant length scales of the problem ranging from the length of the device (~ 5 cm) down to the thickness of the viscous boundary layers (~ 0.5 μm) in the fluid, the latter being responsible for the formation of the steady acoustic streaming. Whereas the pressure acoustics, and thus the acoustic radiation force that dominates the dynamics of large particles ($\gtrsim 2$ μm) suspended in the fluid, depends on the acoustic

*Contact author: shoque@dtu.dk

†Contact author: bruus@fysik.dtu.dk

Published by the American Physical Society under the terms of the *Creative Commons Attribution 4.0 International license*. Further distribution of this work must maintain attribution to the author(s) and the published article's title, journal citation, and DOI.

wavelength ($\sim 500 \mu\text{m}$) and not on the acoustic streaming, the dynamics of submicron particles is dominated by the viscous Stokes drag from the acoustic streaming. The inclusion of the boundary layers in numerical simulations is therefore crucial for a full understanding of acoustofluidic devices and their applications for submicron-particle manipulation in lab-on-a-chip technology [27–30]. Performing direct numerical simulations to capture the entire length-scale range is computationally expensive and poses severe challenges, especially for three-dimensional (3D) simulations.

The effective boundary-layer model introduced by Bach and Bruus in 2018 [31] marked significant progress toward robust modeling of the thin boundary layer. Based on previous work by Nyborg [32], Lee and Wang [33], and Vanneste and Bühler [34], Bach and Bruus derived approximate analytical expressions for the viscous boundary-layer fields that decay exponentially away from the fluid-solid interface inside the thin boundary layer. Inserting these analytic expressions in the governing equations and boundary conditions, an effective model for the remaining bulk acoustic fields was obtained. As these bulk fields do not vary on the small boundary-layer length scale, they can be computed numerically without resolving the boundary layer.

The effective boundary-layer model is based on the assumptions that the boundary-layer thickness δ is much smaller than both the radius of curvature of the fluid-solid interface (the wall) and the acoustic wavelength, and that the amplitude of the wall motion in the perpendicular direction is much smaller than δ . 3D versions of the model have been validated against experimental results in two cases. First, Skov *et al.* [35] used the model to simulate a hard-walled glass-silicon device, and successfully compared their results with previous experimental work [36], regarding both the first-order acoustic fields and the second-order streaming field, although the latter is sensitive to the exact value of the resonance frequency and the detailed shape of the fluid-solid interface. Second, Lickert *et al.* [20] compared simulation results of the model for a soft-walled polymer-based device, and found fairly good agreement with their own experiments regarding the first-order acoustic fields, but no studies of the streaming field were performed.

The main goal of this work is to evaluate the second-order time-averaged streaming field using the boundary-layer model for a soft-walled polymer device. We have found that the second assumption above concerning the smallness of the wall oscillation amplitude compared to δ fails in this case, and therefore an extension of the boundary-layer model is needed to accurately determine the acoustic streaming field for soft-walled devices. In this work, we extend the boundary-layer (BL) model from 2018 by Bach and Bruus [31], henceforth called the “BL18 model,” by allowing for larger perpendicular wall motions.

Introduced in 2025, we call this extended boundary-layer model the “BL25 model.”

The first half of the paper, Secs. II–IV, concerns the development of the theory behind the BL25 model. The basic acoustofluidic perturbation approach as well as the detailed first-order expressions for the acoustic fields carry over unchanged (with one minor addition in a boundary condition) from the BL18 model to the BL25 model, which is summarized in Secs. II and III. In Sec. IV, we present the model of the extended second-order streaming field, where we modify the effective slip-boundary condition by (1) taking into account the hitherto neglected short-range second-order pressure field, and (2) including previously omitted higher-order terms in the small parameter $\epsilon = k_0\delta \simeq 0.003$, k_0 being the acoustic wave number.

The second half of the paper, Secs. V–VIII, concerns the validation of the BL25 model. In Secs. V and VI, respectively, we define the acoustofluidic model devices used for numerical validation of the BL25 model, and we present the implementation of the model for these devices in the finite-element software COMSOL Multiphysics. In Sec. VII, we carry out numerical validations including a mesh-convergence study of the BL25 model in both two-dimensional (2D) and 3D simulations by comparing it to a “Full model” consisting of direct numerical simulation of the full perturbation equations using a mesh that resolves the thin boundary layers. The 3D simulation of the Full model is made possible by studying a downscaled device with a linear size less than $500 \mu\text{m}$, which is driven by a thin-film piezoelectric transducer of thickness $2 \mu\text{m}$. In Sec. VIII, we validate the BL25 model experimentally by using it to model the polymer-device studied by Lickert *et al.* [20] and comparing the simulation results with the published experimental data.

Finally, we end with a summary and concluding remarks in Sec. IX. Some mathematical details are presented in Appendices A–D, and supplementing numerical simulations are provided in the Supplemental Material [37], which also includes Refs. [20,38].

II. PERTURBATION EXPANSION OF THE GOVERNING EQUATIONS

In this work, we follow Bach and Bruus [31] closely, and present here a just summary of the BL18 model, while referring the reader to the original paper for details. We consider a system consisting of a fluid domain Ω^{fl} embedded in an elastic solid domain Ω^{sl} , which is actuated by a piezoelectric transducer domain Ω^{pz} attached to a part $\partial\Omega_{\text{pz}}^{\text{sl}}$ of the outer solid surface $\partial\Omega^{\text{sl}}$ and driven by an applied time-harmonic ac voltage $\varphi_0(t) = \varphi_0 e^{-i\omega t}$ with a real-valued amplitude φ_0 at the angular frequency $\omega = 2\pi f$, where f is the frequency in the megahertz range. The fluid is described by three basic Eulerian fields, the density ρ , the pressure p , and the velocity \mathbf{v} , and the solid by

the basic Lagrangian field, the displacement \mathbf{u} . We assume adiabatic acoustics without thermal transport, so the temperature field is not independent, but follows from the pressure and density.

Assuming a sufficiently low actuation amplitude φ_0 , the whole system can be analyzed using a complex-valued perturbation expansion, where any field g depending on position \mathbf{r} and time t has a uniform constant zeroth-order component g_0 , a time-harmonic first-order component g_1 , and a steady time-averaged second-order component g_2 , proportional to $(\varphi_0)^0$, $(\varphi_0)^1$, and $(\varphi_0)^2$, respectively,

$$g(\mathbf{r}, t) = g_0 + g_1(\mathbf{r})e^{-i\omega t} + g_2(\mathbf{r}), \quad (1a)$$

$$g^{\text{phys}}(\mathbf{r}, t) = g_0 + \text{Re}[g_1(\mathbf{r})e^{-i\omega t}] + g_2(\mathbf{r}). \quad (1b)$$

Here, the physical field $g^{\text{phys}}(\mathbf{r}, t)$ is simply obtained as the real part of the complex-valued field $g(\mathbf{r}, t)$. Note that both the zeroth-order term $g_0(\mathbf{r})$ and the time-averaged second-order terms $g_2(\mathbf{r})$ are real-valued and time-independent. The time average $\langle \dots \rangle$ is defined over a full oscillation period $\tau_0 = 2\pi/\omega$, and the time average of a product of two first-order fields is easily computed using the complex-valued fields,

$$\langle g^{\text{phys}}(\mathbf{r}, t) \rangle = \frac{1}{\tau_0} \int_0^{\tau_0} g^{\text{phys}}(\mathbf{r}, t) dt, \quad (2a)$$

$$\langle A_1^{\text{phys}}(\mathbf{r}, t)B_1^{\text{phys}}(\mathbf{r}, t) \rangle = \frac{1}{2} \text{Re}[A_1(\mathbf{r})B_1^*(\mathbf{r})], \quad (2b)$$

where the asterisk denotes complex conjugation.

A. The linear isotropic elastic solid

We assume that the solid domain Ω^{sl} contains a linear elastic solid with density ρ^{sl} , where the position \mathbf{r} of a solid element with equilibrium position \mathbf{r}_0 is given in terms of the Lagrangian displacement field $\mathbf{u} = \mathbf{u}_1$ as

$$\mathbf{r}(\mathbf{r}_0) = \mathbf{r}_0 + \mathbf{u}_1(\mathbf{r}_0)e^{-i\omega t}, \quad \text{for } \mathbf{r}_0 \in \Omega^{\text{sl}}. \quad (3)$$

This is a first-order expression, since the steady time-averaged second-order displacement \mathbf{u}_2 is neglected, as the steady pressure p_2 in the fluid is too small to deform the surrounding solid noticeably. Using index notation, the governing equation for \mathbf{u}_1 is given by the Cauchy momentum equation in terms of the elastic moduli C_{ik} and the stress tensor σ_1^{sl} with components σ_{1ik}^{sl} [39],

$$u_{1i} = -\frac{1}{\omega^2 \rho^{\text{sl}}} \partial_k \sigma_{1ik}^{\text{sl}}, \quad \text{for } \mathbf{r}_0 \in \Omega^{\text{sl}}, \quad (4a)$$

$$\sigma_{1ik}^{\text{sl}} = C_{44}(\partial_i u_{1k} + \partial_k u_{1i}) + (C_{11} - 2C_{44})\partial_j u_{1j} \delta_{ik}. \quad (4b)$$

At the fluid-solid interface $\partial\Omega_{\text{sl}}^{\text{fl}}$, the equilibrium position is denoted \mathbf{s}_0 , and the interface displacement and

velocity are $\mathbf{s}_1 = \mathbf{u}_1(\mathbf{s}_0)$ and $\mathbf{V}_1^0 = \partial_t \mathbf{s}_1$, respectively,

$$\mathbf{s}(\mathbf{s}_0, t) = \mathbf{s}_0 + \mathbf{s}_1(\mathbf{s}_0)e^{-i\omega t}, \quad \text{for } \mathbf{s}_0 \in \partial\Omega_{\text{sl}}^{\text{fl}}, \quad (5a)$$

$$\partial_t \mathbf{s}(\mathbf{s}_0, t) = -i\omega \mathbf{s}_1(\mathbf{s}_0)e^{-i\omega t} = \mathbf{V}_1^0(\mathbf{s}_0)e^{-i\omega t}. \quad (5b)$$

The boundary conditions on $\partial\Omega_{\text{sl}}^{\text{fl}}$ follow from Eq. (5b), and they are treated further in Sec. II C. The remaining part of $\partial\Omega^{\text{sl}}$ is divided into the free surface $\Omega_{\text{free}}^{\text{sl}}$ and the transducer-solid interface $\Omega_{\text{sl}}^{\text{pz}}$,

$$\sigma_1^{\text{sl}} \cdot \mathbf{n} = \sigma_1^{\text{fl}} \cdot \mathbf{n} \quad \text{and} \quad \mathbf{V}_1^0 = \mathbf{v}_1, \quad \text{for } \mathbf{r} \in \partial\Omega_{\text{sl}}^{\text{fl}}, \quad (6a)$$

$$\sigma_1^{\text{sl}} \cdot \mathbf{n} = \sigma_1^{\text{pz}} \cdot \mathbf{n} \quad \text{and} \quad \mathbf{u}_1^{\text{sl}} = \mathbf{u}_1^{\text{pz}}, \quad \text{for } \mathbf{r} \in \partial\Omega_{\text{sl}}^{\text{pz}}, \quad (6b)$$

$$\sigma_1^{\text{sl}} \cdot \mathbf{n} = \mathbf{0}, \quad \text{for } \mathbf{r} \in \partial\Omega_{\text{free}}^{\text{sl}}. \quad (6c)$$

B. The linear piezoelectric transducer

The linear piezoelectric transducer is described by the elastic deformation \mathbf{u}_1 and the electric potential φ_1 governed by the Cauchy momentum equation and the zero-free-charge Gauss's law for dielectrics coupled by the constitutive equations $\sigma_1^{\text{pz}}(\mathbf{u}_1, \varphi_1)$ and $\mathbf{D}_1(\mathbf{u}_1, \varphi_1)$ for the mechanical stress and electric displacement, respectively, presented in Appendix A,

$$-\rho^{\text{pz}} \omega^2 \mathbf{u}_1 = \nabla \cdot \sigma_1^{\text{pz}}(\mathbf{u}_1, \varphi_1), \quad (7a)$$

$$\mathbf{0} = \nabla \cdot \mathbf{D}_1(\mathbf{u}_1, \varphi_1), \quad (7b)$$

where $\sigma_1^{\text{pz}}(\mathbf{u}_1, \varphi_1)$ and $\mathbf{D}_1(\mathbf{u}_1, \varphi_1)$ are given in Eq. (A2).

The boundary $\partial\Omega^{\text{pz}}$ of Ω^{pz} is divided into three parts: the interface $\Omega_{\text{sl}}^{\text{pz}}$ between Ω^{pz} and Ω^{sl} , the interface $\Omega_{\text{el},n}^{\text{pz}}$ between Ω^{pz} and the n solid electrodes, and the free surface $\Omega_{\text{free}}^{\text{pz}}$. The boundary conditions on each part are

$$\sigma_1^{\text{pz}} \cdot \mathbf{n} = \sigma_1^{\text{sl}} \cdot \mathbf{n}, \quad \mathbf{u}_1^{\text{pz}} = \mathbf{u}_1^{\text{sl}}, \quad \text{and} \quad \varphi_1 = \varphi_0^{(n)}, \quad \text{for } \mathbf{r} \in \partial\Omega_{\text{el},n}^{\text{pz}}, \quad (8a)$$

$$\sigma_1^{\text{pz}} \cdot \mathbf{n} = \sigma_1^{\text{sl}} \cdot \mathbf{n}, \quad \mathbf{u}_1^{\text{pz}} = \mathbf{u}_1^{\text{sl}}, \quad \text{and} \quad \mathbf{n} \cdot \mathbf{D}_1 = 0, \quad \text{for } \mathbf{r} \in \partial\Omega_{\text{sl}}^{\text{pz}}, \quad (8b)$$

$$\sigma_1^{\text{pz}} \cdot \mathbf{n} = \mathbf{0} \quad \text{and} \quad \mathbf{n} \cdot \mathbf{D}_1 = 0, \quad \text{for } \mathbf{r} \in \partial\Omega_{\text{free}}^{\text{pz}}. \quad (8c)$$

C. The Newtonian fluid

We assume that the fluid domain Ω^{fl} contains a Newtonian fluid described by the Eulerian fields, i.e., density ρ , pressure p , and velocity \mathbf{v} , and by the parameters of the unperturbed state, i.e., density ρ_0 , sound speed c_0 , compressibility $\kappa_0 = 1/(\rho_0 c_0^2)$, dynamic viscosity η_0 , and bulk viscosity η_0^b . The governing equations in the adiabatic limit

are the continuity and momentum equations,

$$\partial_t \rho = -\nabla \cdot (\rho \mathbf{v}), \quad (9a)$$

$$\partial_t (\rho \mathbf{v}) = -\nabla \cdot [(\rho \mathbf{v}) \mathbf{v}] + \nabla \cdot \boldsymbol{\sigma}^{\text{fl}}, \quad (9b)$$

where $\boldsymbol{\sigma}^{\text{fl}}$ is the stress tensor with components σ_{ik}^{fl} ,

$$\sigma_{ik}^{\text{fl}} = [-p + (\eta_0^b - \frac{2}{3}\eta_0)\partial_j v_j]\delta_{ik} + \eta_0(\partial_i v_k + \partial_k v_i). \quad (9c)$$

In contrast to the solid domain, the governing equations in the fluid domain are nonlinear, and thus we include the second-order time-averaged fields in the perturbation expansion,

$$\rho = \rho_0 + \rho_1(\mathbf{r})e^{-i\omega t} + \rho_2(\mathbf{r}), \quad (10a)$$

$$p = p_0 + p_1(\mathbf{r})e^{-i\omega t} + p_2(\mathbf{r}), \quad (10b)$$

$$\mathbf{v} = \mathbf{0} + \mathbf{v}_1(\mathbf{r})e^{-i\omega t} + \mathbf{v}_2(\mathbf{r}), \quad \text{for } \mathbf{r} \in \Omega^{\text{fl}}. \quad (10c)$$

The resulting governing equations for first- and second-order perturbation are presented in, respectively, Secs. III and IV below, but already, here, we follow up on Eqs. (5) and formulate the no-slip boundary condition (no-slip BC) $\mathbf{v} = \partial_t \mathbf{s}$ relating the Eulerian fluid velocity \mathbf{v} to the Lagrangian wall velocity $\partial_t \mathbf{s}$, Eq. (5b), at the fluid-solid interface $\partial\Omega_{\text{sl}}^{\text{fl}}$. This condition applies at all times at the actual position $\mathbf{s}(s_0, t)$, Eq. (5a), so we obtain

$$\mathbf{v}(\mathbf{s}_0 + \mathbf{s}_1 e^{-i\omega t}, t) = \mathbf{V}_1^0(\mathbf{s}_0)e^{-i\omega t}, \quad \text{no-slip BC.} \quad (11)$$

Combining Eqs. (10c) and (11) with the Taylor expansion $\mathbf{v}(\mathbf{s}_0 + \mathbf{s}_1, t) \approx \mathbf{v}_1(\mathbf{s}_0)e^{-i\omega t} + \langle (\mathbf{s}_1 \cdot \nabla) \mathbf{v}_1 \rangle|_{\mathbf{s}_0}$, and collecting the terms order by order, gives

$$\mathbf{v}_1(\mathbf{s}_0) = \mathbf{V}_1^0(\mathbf{s}_0), \quad \text{first-order no-slip BC,} \quad (12a)$$

$$\mathbf{v}_2(\mathbf{s}_0) = -\langle (\mathbf{s}_1 \cdot \nabla) \mathbf{v}_1 \rangle|_{\mathbf{s}_0}, \quad \text{second-order no-slip BC.} \quad (12b)$$

D. Surface, boundary-layer, and bulk fields for weakly curved fluid-solid interfaces

A central quantity in acoustofluidic theory is the so-called boundary-layer thickness δ , which is a dynamically defined length scale that appears in the acoustically oscillating fluid inside Ω^{fl} near the fluid-solid interface $\partial\Omega_{\text{sl}}^{\text{fl}}$; see Sec. III. For megahertz ultrasound in water, $\delta \approx 0.5 \mu\text{m}$ is very small compared to the inverse wave number $k_0^{-1} = c_0/\omega \approx 240 \mu\text{m}$, and for weakly curved surfaces it

is also much smaller than the radius of curvature R of $\partial\Omega_{\text{sl}}^{\text{fl}}$,

$$\delta = \sqrt{\frac{2\nu_0}{\omega}}, \quad \text{small boundary length scale,} \quad (13a)$$

$$d = \min\left\{\frac{c_0}{\omega}, R\right\}, \quad \text{large bulk length scale,} \quad (13b)$$

$$\epsilon = \frac{\delta}{d} \ll 1, \quad \text{small length-scale ratio.} \quad (13c)$$

As in BL18, we introduce, for a given point \mathbf{s}_0 at $\partial\Omega_{\text{sl}}^{\text{fl}}$, the orthonormal local coordinates ξ , η , and ζ with their origin at \mathbf{s}_0 , such that ζ is the normal coordinate pointing into Ω^{fl} , $\mathbf{e}_\zeta = -\mathbf{n}(\partial\Omega_{\text{sl}}^{\text{fl}})$, and ξ and η are the coordinates in the tangent plane to $\partial\Omega_{\text{sl}}^{\text{fl}}$ at \mathbf{s}_0 with $\mathbf{e}_\xi \times \mathbf{e}_\eta = \mathbf{e}_\zeta$.

Importantly, for fluid fields in both first- and second-order perturbation, we distinguish between bulk fields \mathcal{A}^d that extend into the bulk with spatial variation on the bulk length scale d and that are typically found by numerical simulation, and boundary-layer fields \mathcal{A}^δ that decay to zero away from the wall on the boundary-layer length scale δ . For the boundary-layer fields, the smallness of the length ratio $\epsilon \sim \delta/d$ allows for separation of variables and simplification of the differential geometrical properties, as summarized in the following expressions, where superscript ‘‘0’’ refers to surface properties that depend only on the in-plane coordinates ξ and η , and where subscript ‘‘||’’ denotes tangential components,

$$\mathcal{A}^\delta(\xi, \eta, \zeta) \approx \mathcal{A}^{\delta 0}(\xi, \eta) a^\delta(\zeta), \quad (14a)$$

$$\text{with } a^\delta(\zeta) \rightarrow 0 \text{ for } \zeta/\delta \rightarrow \infty,$$

$$\mathcal{A}_{||} = A_\xi \mathbf{e}_\xi + A_\eta \mathbf{e}_\eta, \quad (14b)$$

$$\nabla_{||} = \mathbf{e}_\xi \partial_\xi + \mathbf{e}_\eta \partial_\eta, \quad (14c)$$

$$\nabla \cdot \mathcal{A}^0 \approx \nabla_{||} \cdot \mathcal{A}_{||}^0, \quad (14d)$$

$$\mathcal{A}^0 \cdot \nabla \mathcal{B}^0 \approx \mathcal{A}_{||}^0 \cdot (\nabla_{||} \mathcal{B}_{||}^0) \mathbf{e}_i, \quad (14e)$$

$$\nabla^2 a^\delta \approx \partial_\zeta^2 a^\delta, \quad (14f)$$

$$\nabla^2 \mathcal{A}^\delta \approx \mathcal{A}^{\delta 0} \partial_\zeta^2 a(\zeta) = \partial_\zeta^2 \mathcal{A}^\delta, \quad (14g)$$

$$\nabla \cdot \mathcal{A}^\delta \approx \nabla_{||} \cdot \mathcal{A}_{||}^\delta + \partial_\zeta \mathcal{A}_\zeta^\delta. \quad (14h)$$

III. FIRST-ORDER ACOUSTIC FLUID FIELDS

The first step in developing the governing equations (9) for a Newtonian fluid in a first-order time-harmonic perturbation expansion (10) is to use the adiabatic relation between the pressure p_1 and the density ρ_1 ,

$$i\omega \kappa_0 p_1 = \nabla \cdot \mathbf{v}_1, \quad \text{with } p_1 = c_0^2 \rho_1, \quad (15a)$$

$$-i\omega \rho_0 \mathbf{v}_1 = -\nabla p_1 + \beta \eta_0 \nabla(\nabla \cdot \mathbf{v}_1) + \eta_0 \nabla^2 \mathbf{v}_1, \quad (15b)$$

$$\text{with } \beta = \eta_0^b/\eta_0 + \frac{1}{3},$$

where, by using Eq. (9c), the first-order stress σ_1^{fl} has been expressed in terms of the first-order fields p_1 and \mathbf{v}_1 .

We have no changes to the treatment in the BL18 model of the first-order acoustic fields, so this section contains just a brief summary. The second step is to perform a Helmholtz decomposition of the velocity field \mathbf{v}_1 into a curl-free compressible potential-flow component \mathbf{v}_1^d and a divergence-free incompressible component \mathbf{v}_1^δ ,

$$\mathbf{v}_1 = \mathbf{v}_1^d + \mathbf{v}_1^\delta, \quad \text{with } \nabla \times \mathbf{v}_1^d = \mathbf{0} \text{ and } \nabla \cdot \mathbf{v}_1^\delta = 0. \quad (16a)$$

Using Eq. (16) in Eq. (15a) gives $\nabla \cdot \mathbf{v}_1^d = i\omega\kappa_0 p_1$ (\mathbf{v}_1^δ drops out), and inserting this in Eq. (15b) gives

$$-i\omega\rho_0(\mathbf{v}_1^d + \mathbf{v}_1^\delta) = \nabla[-p_1 + (\beta + 1)\eta_0(i\omega\kappa_0 p_1)] + \eta_0 \nabla^2 \mathbf{v}_1^\delta, \quad (16b)$$

where we have used $\nabla^2 \mathbf{v}_1^d = \nabla(\nabla \cdot \mathbf{v}_1^d)$.

Now, \mathbf{v}_1^δ is seen to obey a Helmholtz equation with a strongly damped shear wave number k_s , whereas \mathbf{v}_1^d is proportional to ∇p_1 , which upon taking the divergence becomes another Helmholtz equation with the weakly damped compression wave number k_c ,

$$\mathbf{v}_1^d = -i \frac{1 - i\Gamma}{\omega\rho_0} \nabla p_1, \quad \text{with } \Gamma = \frac{(1 + \beta)\eta_0\omega}{\rho_0 c_0^2}, \quad (17a)$$

$$\nabla \cdot \mathbf{v}_1^d = i\omega\kappa_0 p_1, \quad (17b)$$

$$\nabla^2 p_1 = -k_c^2 p_1, \quad \text{with } k_c = \left(1 + i\frac{\Gamma}{2}\right)k_0, \quad k_0 = \frac{\omega}{c_0}, \quad (17c)$$

$$\nabla^2 \mathbf{v}_1^\delta = -k_s^2 \mathbf{v}_1^\delta, \quad \text{with } k_s = \frac{1 + i}{\delta}, \quad \delta = \sqrt{\frac{2\nu_0}{\omega}}. \quad (17d)$$

We note that it is through the Helmholtz equation (17d) with its exponentially decaying solutions due to the shear wave number k_s that the notion of boundary layers of width δ enters the theory. We also note that the damping coefficient Γ in the compression wave number k_c is of second order in the small parameter ϵ of Eq. (13c), $\Gamma = \frac{1}{2}(1 + \beta)\epsilon^2 \ll 1$, indeed a weak damping.

Although of second order, the average acoustic energy density E_{ac} of the fluid occupying the volume V_{fl} and the time-averaged acoustic radiation force \mathbf{F}^{rad} on a suspended particle of radius a and scattering coefficients f_0 and f_1 are given directly by the first-order fields as [20]

$$E_{\text{ac}} = \frac{1}{V_{\text{fl}}} \int_{V_{\text{fl}}} \left[\frac{1}{4}\kappa_0 |p_1|^2 + \frac{1}{4}\rho_0 |\mathbf{v}_1|^2 \right] dV, \quad (18a)$$

$$\mathbf{F}^{\text{rad}} = \pi a^3 \nabla \left[\frac{1}{3}f_0 \kappa_0 |p_1|^2 - \frac{1}{2}f_1 \frac{1}{4}\rho_0 |\mathbf{v}_1|^2 \right]. \quad (18b)$$

A. The analytical first-order boundary-layer field

For weakly curved, thin boundary layers, discussed in Sec. IID, the analytical form of the incompressible velocity field \mathbf{v}_1^δ is easily found from Eq. (17d) to be

$$\mathbf{v}_1^\delta = \mathbf{v}_1^{\delta 0}(\xi, \eta) e^{ik_s \zeta} + \mathcal{O}(\epsilon), \quad (19a)$$

$$\mathbf{v}_1^{\delta 0} = \mathbf{V}_1^0 - \mathbf{v}_1^{d0}, \quad \text{first-order no-slip BC.} \quad (19b)$$

Here, by combining Eqs. (12) and (16), the amplitude $\mathbf{v}_1^{\delta 0}(\xi, \eta)$ of \mathbf{v}_1^δ on the surface $\zeta = 0$ is expressed as the difference between the oscillation velocity $\mathbf{V}_1^0(\xi, \eta)$ of the wall and the value $\mathbf{v}_1^{d0}(\xi, \eta)$ of the compressible (acoustic) velocity field \mathbf{v}_1^d at the surface. Note how $\mathbf{v}_1^\delta = \mathbf{v}_1^{\delta 0} e^{i\zeta/\delta} e^{-\zeta/\delta}$ decays exponentially on the small length scale δ in the ζ direction normal to the wall.

B. Boundary condition for the first-order pressure

A crucial relation in the BL18 model is the expression for the normal component $v_{1\zeta}^{\delta 0}$ of $\mathbf{v}_1^{\delta 0}$ on the surface in terms of the wall velocity \mathbf{V}^0 and the bulk acoustic velocity \mathbf{v}_1^{d0} , which follows from the incompressibility condition (16) and the analytical form (19),

$$v_{1\zeta}^{\delta 0} = \frac{i}{k_s} \nabla_{\parallel} \cdot \mathbf{v}_{1\parallel}^{\delta 0} = \frac{i}{k_s} \nabla_{\parallel} \cdot \mathbf{V}_{1\parallel}^0 - \frac{i}{k_s} \nabla_{\parallel} \cdot \mathbf{v}_{1\parallel}^{d0}. \quad (20)$$

Using this result, the boundary condition $v_{1\zeta}^{d0} = \mathbf{V}_{1\zeta}^0 - v_{1\zeta}^{\delta 0}$ for the bulk field at the surface takes the self-consistent form to leading order in $\delta = (1 + i)/k_s$,

$$v_{1\zeta}^{d0} = \left(\mathbf{V}_{1\zeta}^0 - \frac{i}{k_s} \nabla_{\parallel} \cdot \mathbf{V}_{1\parallel}^0 \right) + \frac{i}{k_s} \nabla_{\parallel} \cdot \mathbf{v}_{1\parallel}^{d0}. \quad (21)$$

Writing this first-order velocity boundary condition (BC) in terms of the pressure p_1 , using $\nabla_{\parallel} \cdot \mathbf{v}_{1\parallel}^{d0} = \nabla \cdot \mathbf{v}_1^{d0} - \partial_{\zeta} v_{1\zeta}^{d0}$ and Eq. (17a), leads to the self-consistent boundary condition for the first-order pressure p_1 in the BL18 model,

$$\partial_{\zeta} p_1 = \frac{i\omega\rho_0}{1 - i\Gamma} \left(\mathbf{V}_{1\zeta}^0 - \frac{i}{k_s} \nabla_{\parallel} \cdot \mathbf{V}_{1\parallel}^0 \right) - \frac{i}{k_s} (k_c^2 p_1 + \partial_{\zeta}^2 p_1), \quad \text{first-order pressure BC at } \Omega^{\text{fl}}. \quad (22)$$

C. Boundary condition for the first-order stress

The first-order stress condition $\sigma^{\text{sl}} \cdot \mathbf{e}_{\zeta} = \sigma_1^{\text{fl}} \cdot \mathbf{e}_{\zeta}$ at the interface $\partial\Omega_{\text{sl}}^{\text{fl}}$ with inward surface normal \mathbf{e}_{ζ} is rewritten by combining the first-order part σ_1^{fl} of σ^{fl} , Eq. (9c), with the first-order expressions Eqs. (16), (17), and (19). Keeping terms to leading order in $k_0\delta$ leads to the first-order

stress boundary condition of the BL18 model,

$$\begin{aligned}\boldsymbol{\sigma}_1^{\text{sl}} \cdot \mathbf{e}_\zeta &= -p_1 \mathbf{e}_\zeta + ik_s \eta_0 (\mathbf{V}_{1\parallel}^0 - \mathbf{v}_{1\parallel}^d) \\ &\quad + ik_s \eta_0 2(V_{1\zeta}^0 - v_{1\zeta}^d) \mathbf{e}_\zeta, \\ &= -p_1 \mathbf{e}_\zeta + ik_s \eta_0 [\mathbf{V}_1^0 - \mathbf{v}_1^d + (V_{1\zeta}^0 - v_{1\zeta}^d) \mathbf{e}_\zeta],\end{aligned}\quad (23)$$

first-order stress BC at Ω^{fl} ,

where in the last expression we have used $\mathbf{v} = \mathbf{v}_\parallel + v_\zeta \mathbf{e}_\zeta$. Since $k_s \eta_0 = ((1+i)/\delta) \eta_0 = ((1+i)/2) k_0 \delta \rho_0 c_0$, Eq. (23) is the usual pressure condition plus a correction term of order $k_0 \delta = \epsilon$ due to the viscous stress $\eta_0 \partial_\zeta v_1^\delta$ in the boundary layer. The last term in Eq. (23) was left out in the BL18 model.

IV. SECOND-ORDER TIME-AVERAGED STREAMING FIELDS IN THE FLUID

We compute the time-averaged acoustic streaming by second-order perturbation theory, closely following the BL18 model but now extending it in the BL25 model by keeping terms of higher order in $k_0 \delta$ hitherto neglected. The time-averaged part of the governing equations and the boundary conditions in second-order perturbation are obtained from Eqs. (9) and (12),

$$\rho_0 \nabla \cdot \mathbf{v}_2 = -\nabla \cdot \langle \rho_1, \mathbf{v}_1 \rangle, \quad (24a)$$

$$\nabla \cdot \boldsymbol{\sigma}_2^{\text{fl}} = \rho_0 \nabla \cdot \langle \mathbf{v}_1, \mathbf{v}_1 \rangle, \quad (24b)$$

$$\mathbf{v}_2^0 = -\frac{1}{\omega} \langle i \mathbf{v}_1^0 \cdot \nabla, \mathbf{v}_1^0 \rangle, \quad (24c)$$

where we have followed Eqs. (10) and dropped $\langle \cdot \rangle$ from the time-averaged velocity \mathbf{v}_2 , pressure p_2 , and stress $\boldsymbol{\sigma}_2^{\text{fl}}$.

Equations (24) represent a compressible Stokes-flow problem in the second-order fields \mathbf{v}_2 and $\boldsymbol{\sigma}_2^{\text{fl}}$, where the known first-order fields act as source terms. This problem is split in two parts: the second-order boundary-layer fields driven by the short-range source terms, $\nabla \cdot \langle \rho_1 \mathbf{v}_1^\delta \rangle$ and $\rho_0 \nabla \cdot \langle \mathbf{v}_1^\delta \mathbf{v}_1^\delta + \mathbf{v}_1^\delta \mathbf{v}_1^d + \mathbf{v}_1^d \mathbf{v}_1^\delta \rangle$, and the second-order bulk streaming field driven by the long-range source terms, $\nabla \cdot \langle \rho_1 \mathbf{v}_1^d \rangle$ and $\rho_0 \nabla \cdot \langle \mathbf{v}_1^d \mathbf{v}_1^d \rangle$. The corresponding responses are long-range bulk fields (superscript “ d ”) and short-range boundary-layer fields (superscript “ δ ”),

$$\mathbf{v}_2 = \mathbf{v}_2^d + \mathbf{v}_2^\delta, \quad \text{for } \mathbf{r} \in \partial\Omega_{\text{sl}}^{\text{fl}}, \quad (25a)$$

$$p_2 = p_2^d + p_2^\delta, \quad \text{for } \mathbf{r} \in \partial\Omega_{\text{sl}}^{\text{fl}}, \quad (25b)$$

$$\boldsymbol{\sigma}_2^{\text{fl}} = \boldsymbol{\sigma}_2^d + \boldsymbol{\sigma}_2^\delta, \quad \text{for } \mathbf{r} \in \partial\Omega_{\text{sl}}^{\text{fl}}, \quad (25c)$$

$$\mathbf{v}_2^{d0} = -\mathbf{v}_2^{\delta0} - \langle (\mathbf{s}_1 \cdot \nabla) \mathbf{v}_1 \rangle, \quad \text{for } \mathbf{r} = \mathbf{s}_0. \quad (25d)$$

A. Short-range boundary-layer streaming

The governing equations for the second-order boundary-layer fields, \mathbf{v}_2^δ , p_2^δ , and $\boldsymbol{\sigma}_2^\delta$, are obtained by collecting the

terms of Eqs. (24) that contain at least one short-range first-order field \mathbf{v}_1^δ ,

$$\nabla \cdot (\rho_0 \mathbf{v}_2^\delta) = -\nabla \cdot \langle \rho_1 \mathbf{v}_1^\delta \rangle, \quad (26a)$$

$$\nabla \cdot \boldsymbol{\sigma}_2^\delta = \rho_0 \nabla \cdot \langle \mathbf{v}_1^\delta \mathbf{v}_1^\delta + \mathbf{v}_1^\delta \mathbf{v}_1^d + \mathbf{v}_1^d \mathbf{v}_1^\delta \rangle, \quad (26b)$$

$$\text{with } \nabla \cdot \boldsymbol{\sigma}_2^\delta = \nabla(-p_2^\delta + \beta \eta_0 \nabla \cdot \mathbf{v}_2^\delta) + \eta_0 \nabla^2 \mathbf{v}_2^\delta, \quad (26c)$$

$$\text{where } \mathbf{v}_2^\delta \rightarrow \mathbf{0} \text{ and } p_2^\delta \rightarrow 0 \text{ as } \zeta \rightarrow \infty. \quad (26d)$$

Thus \mathbf{v}_2^δ , p_2^δ , and $\boldsymbol{\sigma}_2^\delta$ are driven by source terms containing time-average products of first-order terms of the form $\langle \mathbf{A}_1, \mathbf{B}_1 \rangle$, where \mathbf{A}_1 and \mathbf{B}_1 are either \mathbf{v}_1^d or \mathbf{v}_1^δ .

To solve Eqs. (26), we first combine Eqs. (26b) and (26c) to obtain the Laplacian of \mathbf{v}_2^δ ,

$$\begin{aligned}\eta_0 \nabla^2 \mathbf{v}_2^\delta &= -\beta \eta_0 \nabla (\nabla \cdot \mathbf{v}_2^\delta) + \nabla p_2^\delta \\ &\quad + \rho_0 \nabla \cdot \langle \mathbf{v}_1^\delta \mathbf{v}_1^\delta + \mathbf{v}_1^d \mathbf{v}_1^\delta + \mathbf{v}_1^\delta \mathbf{v}_1^d \rangle.\end{aligned}\quad (27a)$$

We note that Eq. (14f) gives $\nabla^2 \mathbf{v}_2^\delta \approx \partial_\zeta^2 \mathbf{v}_2^\delta$, and that using Eq. (26a) the divergence term is rewritten as

$$\begin{aligned}-\beta \eta_0 \nabla (\nabla \cdot \mathbf{v}_2^\delta) &= \beta v_0 \nabla \langle \mathbf{v}_1^\delta \cdot \nabla \rho_1 \rangle \\ &= \frac{\beta \eta_0 \omega}{c_0^2} \nabla \langle \mathbf{v}_1^\delta \cdot (i \mathbf{v}_1^d) \rangle.\end{aligned}\quad (27b)$$

This term is neglected, as it is smaller by a factor Γ compared to the other divergence term. In the BL18 model, the short-range second-order pressure field p_2^δ was also neglected, since the perpendicular velocity of the wall was assumed to be small.

However, a major point in the BL25 model is that we relax this assumption and keep p_2^δ . Thus, we end with two source terms for \mathbf{v}_2^δ , which therefore is split in two corresponding terms,

$$\mathbf{v}_2^\delta = \mathbf{v}_2^{\delta p} + \mathbf{v}_2^{\delta v}, \quad (28a)$$

$$\text{where } \mathbf{v}_2^{\delta p}(\xi, \eta, \infty) = \mathbf{v}_2^{\delta v}(\xi, \eta, \infty) = \mathbf{0},$$

$$\partial_\zeta^2 \mathbf{v}_2^{\delta p} = \frac{1}{\eta_0} \nabla p_2^\delta, \quad (28b)$$

$$\partial_\zeta^2 \mathbf{v}_2^{\delta v} = \frac{1}{v_0} \nabla \cdot \langle \mathbf{v}_1^\delta \mathbf{v}_1^\delta + \mathbf{v}_1^d \mathbf{v}_1^\delta + \mathbf{v}_1^\delta \mathbf{v}_1^d \rangle. \quad (28c)$$

An analytical expression for \mathbf{v}_2^δ is derived by separating the first-order fields in the source terms into the parallel coordinates (ξ, η) and the perpendicular coordinate ζ ,

$$\mathbf{A}_1 = a(\zeta) \mathbf{A}_1^0(\xi, \eta), \quad (29a)$$

$$\mathbf{B}_1 = b(\zeta) \mathbf{B}_1^0(\xi, \eta), \quad (29b)$$

$$\langle \mathbf{A}_1, \mathbf{B}_1 \rangle = \langle a\mathbf{A}_1^0, b\mathbf{B}_1^0 \rangle = \langle ab^* \mathbf{A}_1^0, \mathbf{B}_1^0 \rangle, \quad (29c)$$

with $\langle \mathbf{A}_1, \mathbf{B}_1 \rangle = \langle \mathbf{A}_1 \mathbf{B}_1 \rangle$.

Here, in the last expression, we have introduced the comma-separated notation $\langle \mathbf{A}_1, \mathbf{B}_1 \rangle = \langle \mathbf{A}_1 \mathbf{B}_1 \rangle$ to ensure clarity when moving prefactors back and forth between \mathbf{A}_1^0 and \mathbf{B}_1^0 , such as when collecting all ζ dependence in the product $a(\zeta)b^*(\zeta)$.

The appearance of the simplified Laplacian (14f), $\nabla^2 g^\delta \approx \partial_\zeta^2 g^\delta$, in the boundary-layer equations (26) implies that we need to integrate terms $\langle \mathbf{A}_1, \mathbf{B}_1 \rangle$ with respect to ζ . To this end, as in the BL18 model, we introduce the recursive n -fold integrals $I_{ab}^{(n)}(\zeta)$ for integer values $n = 1, 2, 3, \dots$, and for the extensions $n = 0$ (no integration) and $-n$ (the n th derivative),

$$I_{ab}^{(0)}(\zeta) = a(\zeta)b(\zeta)^*, \quad \lim_{\zeta \rightarrow \infty} [a(\zeta)b(\zeta)^*] = 0, \quad (30a)$$

$$I_{ab}^{(n)}(\zeta) = \int_\infty^\zeta d\xi I_{ab}^{(n-1)}(\xi), \quad n = 1, 2, 3, \dots, \quad (30b)$$

$$I_{ab}^{(-n)}(\zeta) = \partial_\zeta^n [a(\zeta)b(\zeta)^*], \quad n = 1, 2, 3, \dots, \quad (30c)$$

$$I_{ba}^{(n)}(\zeta) = [I_{ab}^{(n)}(\zeta)]^*, \quad \pm n = 0, 1, 2, 3, \dots, \quad (30d)$$

$$\langle \mathbf{A}_1, \mathbf{B}_1 \rangle = \left\langle I_{ab}^{(0)}(\zeta) \mathbf{A}_1^0(\xi, \eta), \mathbf{B}_1^0(\xi, \eta) \right\rangle. \quad (30e)$$

We also need the coordinate-separated expressions for the i th component $[\nabla \cdot \langle \mathbf{A}_1, \mathbf{B}_1 \rangle]_i$ of the single divergence $\nabla \cdot \langle \mathbf{A}_1, \mathbf{B}_1 \rangle$,

$$\begin{aligned} [\nabla \cdot \langle \mathbf{A}_1, \mathbf{B}_1 \rangle]_i &= \nabla \cdot \left\langle I_{ab}^{(0)}(\zeta) \mathbf{A}_{1i}^0, \mathbf{B}_1^0 \right\rangle \\ &= \nabla_\parallel \cdot \left\langle I_{ab}^{(0)}(\zeta) \mathbf{A}_{1\parallel}^0, \mathbf{B}_{1\parallel}^0 \right\rangle + \left\langle I_{ab}^{(-1)}(\zeta) \mathbf{A}_{1i}^0, \mathbf{B}_{1\zeta}^0 \right\rangle, \end{aligned} \quad (31a)$$

with tangential and normal components

$$\begin{aligned} [\nabla \cdot \langle \mathbf{A}_1, \mathbf{B}_1 \rangle]_\parallel &= \nabla_\parallel \cdot \left\langle I_{ab}^{(0)}(\zeta) \mathbf{A}_{1\parallel}^0, \mathbf{B}_{1\parallel}^0 \right\rangle + \left\langle I_{ab}^{(-1)}(\zeta) \mathbf{A}_{1\parallel}^0, \mathbf{B}_{1\zeta}^0 \right\rangle, \end{aligned} \quad (31b)$$

$$\begin{aligned} [\nabla \cdot \langle \mathbf{A}_1, \mathbf{B}_1 \rangle]_\zeta &= \nabla_\parallel \cdot \left\langle I_{ab}^{(0)}(\zeta) \mathbf{A}_{1\zeta}^0, \mathbf{B}_{1\parallel}^0 \right\rangle + \left\langle I_{ab}^{(-1)}(\zeta) \mathbf{A}_{1\zeta}^0, \mathbf{B}_{1\zeta}^0 \right\rangle, \end{aligned} \quad (31c)$$

and for the double divergence $\nabla \cdot [\nabla \cdot \langle \mathbf{A}_1, \mathbf{B}_1 \rangle]$,

$$\begin{aligned} \nabla \cdot [\nabla \cdot \langle \mathbf{A}_1, \mathbf{B}_1 \rangle] &= \partial_i \left[\nabla_\parallel \cdot \left\langle I_{ab}^{(0)}(\zeta) \mathbf{A}_{1i}^0, \mathbf{B}_{1\parallel}^0 \right\rangle + \left\langle I_{ab}^{(-1)}(\zeta) \mathbf{A}_{1i}^0, \mathbf{B}_{1\zeta}^0 \right\rangle \right] \\ &= \nabla_\parallel \cdot \left[\nabla_\parallel \cdot \left\langle I_{ab}^{(0)}(\zeta) \mathbf{A}_{1\parallel}^0, \mathbf{B}_{1\parallel}^0 \right\rangle + \left\langle I_{ab}^{(-2)}(\zeta) \mathbf{A}_{1\zeta}^0, \mathbf{B}_{1\zeta}^0 \right\rangle \right] \\ &\quad + \nabla_\parallel \cdot \left[\left\langle I_{ab}^{(-1)}(\zeta) \mathbf{A}_{1\parallel}^0, \mathbf{B}_{1\zeta}^0 \right\rangle + \left\langle I_{ab}^{(-1)}(\zeta) \mathbf{A}_{1\zeta}^0, \mathbf{B}_{1\parallel}^0 \right\rangle \right]. \end{aligned} \quad (31d)$$

Using the solution (19a) for \mathbf{v}_1^δ and a first-order Taylor expansion in ζ of \mathbf{v}_1^d valid in the boundary layer $\zeta \ll d$, we obtain the explicit coordinate-separated form for the relevant velocity fields in the boundary layer,

$$\mathbf{v}_1^\delta = q(\zeta) \mathbf{v}_1^{\delta 0}(\xi, \eta), \quad \text{with } q(\zeta) = e^{iks\zeta}, \quad (32a)$$

$$\mathbf{v}_1^d = \mathbf{v}_1^{d0} + \zeta \partial_\zeta \mathbf{v}_1^{d0}, \quad \text{with } \partial_\zeta \mathbf{v}_1^{d0} = \lim_{\zeta \rightarrow 0} \partial_\zeta \mathbf{v}_1^d. \quad (32b)$$

We now see that the functions $a(\zeta)$ and $b(\zeta)$ of Eqs. (29) in the source terms of Eqs. (26) are either $q(\zeta)$, ζ , or unity, and that each product $a(\zeta)b(\zeta)$ contains at least one decaying factor $q(\zeta)$, so the zero-at-infinity boundary condition (30a) is fulfilled. On the surface $\zeta = 0$, $I_{ab}^{(n)}(\zeta)$ becomes $\hat{I}_{ab}^{(n)} = I_{ab}^{(n)}(0)$, which leads to the explicit values,

$$\hat{I}_{qq}^{(-1)} = 0, \quad \hat{I}_{q1}^{(-1)} = \frac{-1+i}{\delta}, \quad \hat{I}_{q\zeta}^{(-1)} = 1, \quad (33)$$

$$\hat{I}_{qq}^{(0)} = 1, \quad \hat{I}_{q1}^{(0)} = 1, \quad \hat{I}_{q\zeta}^{(0)} = 0,$$

$$\hat{I}_{qq}^{(1)} = -\frac{1}{2}\delta, \quad \hat{I}_{q1}^{(1)} = -\frac{1+i}{2}\delta, \quad \hat{I}_{q\zeta}^{(1)} = -\frac{i}{2}\delta^2,$$

$$\hat{I}_{qq}^{(2)} = \frac{1}{4}\delta^2, \quad \hat{I}_{q1}^{(2)} = \frac{i}{2}\delta^2, \quad \hat{I}_{q\zeta}^{(2)} = -\frac{1-i}{2}\delta^3,$$

$$\hat{I}_{qq}^{(3)} = -\frac{1}{8}\delta^3, \quad \hat{I}_{q1}^{(3)} = \frac{1-i}{4}\delta^3, \quad \hat{I}_{q\zeta}^{(3)} = \frac{3}{4}\delta^4,$$

$$\hat{I}_{qq}^{(4)} = \frac{1}{16}\delta^4, \quad \hat{I}_{q1}^{(4)} = -\frac{1}{4}\delta^4, \quad \hat{I}_{q\zeta}^{(4)} = -\frac{1+i}{2}\delta^5.$$

We can now find the analytical solution for \mathbf{v}_2^δ to be used in the slip boundary condition (25a) for the bulk streaming velocity \mathbf{v}_2^{d0} at the wall, $\zeta = 0$. As shown in Appendix B, \mathbf{v}_2^δ is found by integrating Eq. (28) twice from $\zeta = \infty$, where it is zero, to ζ using that: (1) the right-hand side of Eq. (28), called f^{rhs} , can be separated in the in-plane and perpendicular coordinates (ξ, η) and ζ , respectively; (2) f^{rhs} forms a linear superposition of functions $f_\alpha^{\text{rhs}}(\xi, \eta) I_{ab}^{(n_\alpha)}(\zeta)$, $\alpha = 1, 2, \dots, M$; and (3) the functions $I_{ab}^{(n_\alpha)}(\zeta)$ have the special properties summarized in Eqs. (30), notably the integration property (30b) that changes a ζ integration into a simple increase by unity of the index n_α . The structure of the computation of \mathbf{v}_2^δ is simply (see details in Appendix B),

$$\partial_\zeta^2 \mathbf{v}_2^\delta = \sum_{\alpha=1}^M f_\alpha^{\text{rhs}}(\xi, \eta) I_{ab}^{(n_\alpha)}(\zeta), \quad (34a)$$

which implies

$$\mathbf{v}_2^\delta = \sum_{\alpha=1}^M f_\alpha^{\text{rhs}}(\xi, \eta) I_{ab}^{(n_\alpha+2)}(\zeta). \quad (34b)$$

The surface value $v_2^{\delta 0}$ of the boundary-layer field \mathbf{v}_2^δ is derived in Appendix B in terms of its tangential and normal components, including the prefactor $1/v_0 = \frac{2}{\omega\delta^2}$, and by substituting the bulk factors $I_{ab}^{(n)}(\zeta)$ with their surface values $\hat{I}_{ab}^{(n)}$ given in Eq. (33), with $\frac{2}{\omega\delta^2}\hat{I}_{qq}^{(n)}, \frac{2}{\omega\delta^2}\hat{I}_{1q}^{(n)} \propto \delta^{n-2}$, and $\frac{2}{\omega\delta^2}\hat{I}_{\zeta q}^{(n)} \propto \delta^{n-1}$. The result is

$$\mathbf{v}_2^{\delta 0} = \mathbf{v}_{2\parallel}^{\delta 0} + v_{2\zeta}^{\delta 0} \mathbf{e}_\zeta, \quad (35a)$$

$$\begin{aligned} v_{2\parallel}^{\delta 0} = & \frac{2}{\omega\delta^2} \left\{ -\nabla_{\parallel} \left[\left\langle \hat{I}_{qq}^{(2)} \mathbf{v}_{1\zeta}^{\delta 0}, \mathbf{v}_{1\zeta}^{\delta 0} \right\rangle + \left\langle \hat{I}_{1q}^{(2)} \mathbf{v}_{1\zeta}^{d0}, \mathbf{v}_{1\zeta}^{\delta 0} \right\rangle \right. \right. \\ & + \left. \left. \left\langle \hat{I}_{q1}^{(2)} \mathbf{v}_{1\zeta}^{\delta 0}, \mathbf{v}_{1\zeta}^{d0} \right\rangle \right] \right. \\ & + \nabla_{\parallel} \cdot \left\langle \hat{I}_{qq}^{(2)} \mathbf{v}_{1\parallel}^{\delta 0}, \mathbf{v}_{1\parallel}^{\delta 0} \right\rangle + \left\langle \hat{I}_{qq}^{(1)} \mathbf{v}_{1\parallel}^{\delta 0}, \mathbf{v}_{1\zeta}^{\delta 0} \right\rangle \\ & + \nabla_{\parallel} \cdot \left\langle \hat{I}_{1q}^{(2)} \mathbf{v}_{1\parallel}^{d0}, \mathbf{v}_{1\parallel}^{\delta 0} \right\rangle + \left\langle \hat{I}_{1q}^{(1)} \mathbf{v}_{1\parallel}^{d0}, \mathbf{v}_{1\zeta}^{\delta 0} \right\rangle \\ & + \nabla_{\parallel} \cdot \left\langle \hat{I}_{q1}^{(2)} \mathbf{v}_{1\parallel}^{\delta 0}, \mathbf{v}_{1\parallel}^{d0} \right\rangle + \left\langle \hat{I}_{q1}^{(1)} \mathbf{v}_{1\parallel}^{\delta 0}, \mathbf{v}_{1\zeta}^{\delta 0} \right\rangle \\ & \left. + \left\langle \hat{I}_{\zeta q}^{(1)} \partial_\zeta \mathbf{v}_{1\parallel}^{d0}, \mathbf{v}_{1\zeta}^{\delta 0} \right\rangle + \left\langle \hat{I}_{q\zeta}^{(1)} \mathbf{v}_{1\parallel}^{\delta 0}, \partial_\zeta \mathbf{v}_{1\zeta}^{d0} \right\rangle \right\}, \quad (35b) \end{aligned}$$

$$\begin{aligned} v_{2\zeta}^{\delta 0} = & -\frac{2}{\omega\delta^2} \left\{ +\nabla_{\parallel} \cdot \left[\nabla_{\parallel} \cdot \left\langle \hat{I}_{qq}^{(3)} \mathbf{v}_{1\parallel}^{\delta 0}, \mathbf{v}_{1\parallel}^{\delta 0} \right\rangle + \left\langle \hat{I}_{qq}^{(2)} \mathbf{v}_{1\parallel}^{\delta 0}, \mathbf{v}_{1\zeta}^{\delta 0} \right\rangle \right] \right. \\ & + \nabla_{\parallel} \cdot \left[\nabla_{\parallel} \cdot \left\langle \hat{I}_{1q}^{(3)} \mathbf{v}_{1\parallel}^{d0}, \mathbf{v}_{1\parallel}^{\delta 0} \right\rangle + \left\langle \hat{I}_{1q}^{(2)} \mathbf{v}_{1\parallel}^{d0}, \mathbf{v}_{1\zeta}^{\delta 0} \right\rangle \right] \\ & + \nabla_{\parallel} \cdot \left[\nabla_{\parallel} \cdot \left\langle \hat{I}_{q1}^{(3)} \mathbf{v}_{1\parallel}^{\delta 0}, \mathbf{v}_{1\parallel}^{d0} \right\rangle + \left\langle \hat{I}_{q1}^{(2)} \mathbf{v}_{1\parallel}^{\delta 0}, \mathbf{v}_{1\zeta}^{d0} \right\rangle \right] \\ & \left. + \nabla_{\parallel} \cdot \left[\left\langle \hat{I}_{\zeta q}^{(2)} \partial_\zeta \mathbf{v}_{1\parallel}^{d0}, \mathbf{v}_{1\zeta}^{\delta 0} \right\rangle + \left\langle \hat{I}_{q\zeta}^{(2)} \mathbf{v}_{1\parallel}^{\delta 0}, \partial_\zeta \mathbf{v}_{1\zeta}^{d0} \right\rangle \right] \right\}. \quad (35c) \end{aligned}$$

Here, terms to the two lowest powers in the small length scale δ are kept, which for Eq. (35b) are δ^{-1} and δ^0 , and for Eq. (35c) are δ^0 and δ^1 . These expressions for $\mathbf{v}_2^{\delta 0}$ are central in the BL25 model. In BL18 only the lowest power δ^{-1} in Eq. (35b) and δ^0 in Eq. (35c) was kept.

B. Long-range bulk streaming

The governing equations for the second-order bulk streaming follow from the long-range part of Eqs. (24), and they are the same as in the BL18 model,

$$\rho_0 \nabla \cdot \mathbf{v}_2^d = \nabla \cdot \langle \rho_1 \mathbf{v}_1^d \rangle, \quad (36a)$$

$$\begin{aligned} \nabla \cdot \boldsymbol{\sigma}_2^d &= \rho_0 \nabla \cdot \langle \mathbf{v}_1^d \mathbf{v}_1^d \rangle \\ &= \rho_0 \langle \mathbf{v}_1^d \cdot \nabla \mathbf{v}_1^d \rangle + \rho_0 \langle \mathbf{v}_1^d \nabla \cdot \mathbf{v}_1^d \rangle, \quad (36b) \end{aligned}$$

$$\text{with } \nabla \cdot \boldsymbol{\sigma}_2^d = -\nabla (p_2^d - \beta \eta_0 \nabla \cdot \mathbf{v}_2^d) + \eta_0 \nabla^2 \mathbf{v}_2^d. \quad (36c)$$

As shown in Ref. [31], the source terms in these equations can be evaluated using Eqs. (16) and (17),

$$\nabla \cdot \mathbf{v}_2^d = \Gamma \frac{k_0}{2c_0} |\mathbf{v}_1^d|^2 \approx 0, \quad (37a)$$

$$\eta_0 \nabla^2 \mathbf{v}_2^d = \nabla \tilde{p}_2^d - \frac{\Gamma \omega}{c_0^2} \langle p_1^d \mathbf{v}_1^d \rangle, \quad (37b)$$

$$\tilde{p}_2^d = p_2^d - \left(\frac{1}{4} \kappa_0 |\mathbf{p}_1^d|^2 - \frac{1}{4} \rho_0 |\mathbf{v}_1^d|^2 \right), \quad (37c)$$

where we have introduced the excess pressure \tilde{p}_2^d , which is the second-order pressure p_2^d minus the time-averaged acoustic Lagrangian density.

Next, we express the second-order boundary condition (25a), $\mathbf{v}_2^{d0} = -\mathbf{v}_2^{\delta 0} - \langle (\mathbf{s}_1 \cdot \nabla) \mathbf{v}_1 \rangle|_{\zeta=0}$, in terms of the first-order surface values \mathbf{V}_1^0 and \mathbf{v}_1^d of the wall velocity and the bulk acoustic velocity, respectively, noting that by Eq. (19b) we have $\mathbf{v}_1^{\delta 0} = \mathbf{V}_1^0 - \mathbf{v}_1^{d0}$. This has already been achieved for the surface value $\mathbf{v}_2^{\delta 0}$ of the boundary streaming in Eqs. (35); only the Stokes-drift term $\mathbf{v}_2^{\text{sd}} = \langle (\mathbf{s}_1 \cdot \nabla) \mathbf{v}_1 \rangle|_{\zeta=0}$ needs to be treated here. We use Eqs. (12), $\mathbf{s}_1 = (i/\omega)\mathbf{V}_1^0$, and Eqs. (14b) and (32) to compute in-plane and normal derivatives, and obtain

$$\begin{aligned} \mathbf{v}_2^{\text{sd}} &= \langle (\mathbf{s}_1 \cdot \nabla) \mathbf{v}_1 \rangle|_{\zeta=0} \\ &= \frac{1}{\omega} [i(\mathbf{V}_1^0 \cdot \nabla), \mathbf{v}_1^d + \mathbf{v}_1^\delta]|_{\zeta=0} \\ &= \frac{1}{\omega} [i\mathbf{V}_1^0 \cdot \nabla \mathbf{v}_1^{d0} + \nabla_{\parallel} \mathbf{v}_1^{\delta 0}] + \langle \mathbf{V}_1^0, k_s \mathbf{v}_1^{\delta 0} \rangle. \quad (38) \end{aligned}$$

The final form of the slip boundary condition (25a) for \mathbf{v}_2^{d0} is obtained by combining Eqs. (35) and (38),

$$\mathbf{v}_2^{d0} = -(\mathbf{v}_2^{\delta 0} + \mathbf{v}_2^{\text{sd}}) = -(\mathbf{v}_{2\parallel}^{\delta 0} + \mathbf{v}_{2\parallel}^{\text{sd}}) - (v_{2\zeta}^{\delta 0} + v_{2\zeta}^{\text{sd}}) \mathbf{e}_\zeta. \quad (39)$$

In the BL25 model, the second-order steady bulk streaming \mathbf{v}_2^d appears as a weakly compressible Stokes flow governed by Eqs. (37), which is driven by the weak body force $-(\Gamma\omega/c_0^2)\langle p_1^d \mathbf{v}_1^d \rangle$ and by the slip boundary condition (39). All the driving terms have the form of time-averaged products of the first-order fluid pressure and velocity fields p_1 and \mathbf{v}_1 and the first-order solid displacement field \mathbf{u}_1 with wall velocity \mathbf{V}_1^0 as described in Secs. II and III, respectively. In the following section we describe how this model is implemented in COMSOL Multiphysics for numerical solution.

V. ACOUSTOFLUIDIC DEVICE MODELING

We introduce two polymer-based model systems, a 3D device driven by a thin-film transducer and a 2D device driven by a bulk transducer, as sketched in Fig. 1 with the specific geometrical parameters listed in Table I. The

top electrode of the transducer in both models is split by a groove to ensure an efficient excitation of a selected antisymmetric resonance mode.

A. The 3D model with a thin-film transducer

The 3D model is made as small as possible to allow for simulations using the Full model within the available 600-GB-RAM memory capacity of our computer system, while still containing all essential elements of an acoustofluidic device: a fluid cavity (fl) embedded in a solid (sl), which is driven by an attached piezoelectric transducer (pz). Spurious corner effects are avoided by choosing an ellipsoidal fluid domain with principal axes $L_{fl} \gtrsim W_{fl} \gtrsim H_{fl}$, all less than 300 μm . The dimensions of the box-shaped solid of length L_{sl} , width W_{sl} , and height H_{sl} are less than

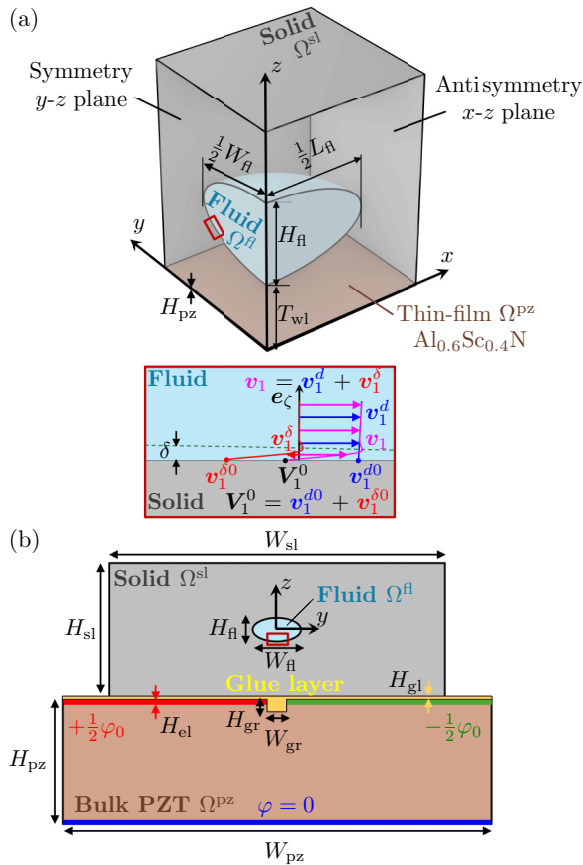


FIG. 1. Two acoustofluidic device models used for numerical validation of the BL25 model against the Full model; see parameter values in Table I. (a) The small submillimeter 3D model consisting of an ellipsoidal fluid domain embedded in a solid with a thin-film $\text{Al}_{0.6}\text{Sc}_{0.4}\text{N}$ transducer attached on its lower surface. (b) The 2D millimeter-sized model consisting of an elliptic fluid domain embedded in a solid, which is attached to a bulk lead-zirconate-titanate transducer via a glue layer. The inset shows an enlargement of the fluid-solid interface that illustrates the Helmholtz decomposition (16) $\mathbf{v}_1 = \mathbf{v}_1^d + \mathbf{v}_1^\delta$ of the acoustic velocity field.

TABLE I. The geometrical parameters for the 3D and 2D polymer-based devices considered here; see also Fig. 1.

Symbol	Value (μm)	Symbol	Value (μm)
<i>3D device driven by an $\text{Al}_{0.6}\text{Sc}_{0.4}\text{N}$ thin-film transducer</i>			
L_{sl}	500	L_{fl}	300
W_{sl}	475	W_{fl}	275
H_{sl}	320	H_{fl}	120
H_{pz}	2	T_{wl}	100
<i>2D device driven by a bulk PZT transducer</i>			
W_{sl}	2750	W_{fl}	392
H_{sl}	650	H_{fl}	351
W_{pz}	3500	W_{gr}	150
H_{pz}	500	H_{gr}	100
H_{el}	9	H_{gl}	20

500 μm , which results in resonance frequencies in the relevant range of 1–2 MHz. The elastic solid is poly(methyl methacrylate) (PMMA), and the smallest possible transducer is a thin-film $\text{Al}_{0.6}\text{Sc}_{0.4}\text{N}$ transducer of height $H_{pz} \simeq 2 \mu\text{m}$, which covers the bottom surface of the solid as studied in Refs. [40,41].

By assuming the y - z and x - z plane to be a symmetry and an antisymmetry plane, respectively, the computational domain is reduced to a quarter of the full domain. The boundary conditions presented in the previous sections therefore need to be supplemented by the following (anti)symmetry-plane conditions valid for each perturbation order.

$$\text{Symmetry at } x = 0 : \quad (40a)$$

$$\partial_x p_1 = 0, \quad \partial_x \varphi_1 = 0, \quad u_{1,x} = 0, \quad \sigma_{1yx}^{sl} = \sigma_{1zx}^{sl} = 0, \quad (40b)$$

$$\partial_x p_2 = 0, \quad v_{2x}^d = 0, \quad \sigma_{2yx}^{d,fl} = \sigma_{2zx}^{d,fl} = 0. \quad (40c)$$

$$\text{Symmetry at } y = 0 : \quad (40d)$$

$$\partial_y p_2 = 0, \quad v_{2y}^d = 0, \quad \sigma_{2xy}^{d,fl} = \sigma_{2zy}^{d,fl} = 0. \quad (40e)$$

$$\text{Antisymmetry at } y = 0 : \quad (40f)$$

$$p_1 = 0, \quad \varphi_1 = 0, \quad \sigma_{1yy}^{sl} = 0, \quad u_{1x} = u_{1z} = 0. \quad (40g)$$

Finally, as there are only a top and a bottom electrode on the transducer in the symmetry-reduced model, the potential boundary condition (8a) becomes

$$\varphi_1 = +\frac{1}{2}\varphi_0, \quad \text{for } \mathbf{r} \in \partial\Omega_{\text{top}}^{\text{pz}}, \quad (41a)$$

$$\varphi_1 = 0, \quad \text{for } \mathbf{r} \in \partial\Omega_{\text{bottom}}^{\text{pz}}. \quad (41b)$$

The 20-nm-thick metal electrodes are not explicitly included in the model, but they appear indirectly through the potential values (41) on the transducer surfaces.

B. The 2D model with a bulk transducer

The 2D model is nearly the same as the cross section of the actual millimeter-sized bulk-transducer-driven polymer-based device studied in Ref. [20]. However, to avoid spurious corner effects in the numerical validation, we have changed the original rectangular fluid domain to a smooth elliptical domain with major axis W_{fl} and minor axis H_{fl} . The rectangular solid and bulk lead-zirconate-titanate (PZT) transducer have width \times height given by $W_{\text{sl}} \times H_{\text{sl}}$ and $W_{\text{pz}} \times H_{\text{pz}}$, respectively. The glue layer between the transducer and the solid has the thickness H_{gl} , the thickness of the electrodes is H_{el} , and the glue-filled groove in the top electrode has width W_{gr} and height H_{gr} . Note that in this model there are three isotropic elastic solid domains with corresponding Cauchy momentum equations (4), i.e., the PMMA wall (sl = pm), the glue layer (sl = gl), and the silver electrodes (sl = el). Also, note that the boundary conditions (6b) according to Fig. 1, instead of only $\partial\Omega_{\text{sl}}^{\text{pz}}$, now include three types of interfaces, i.e., $\partial\Omega_{\text{el}}^{\text{pz}}$, $\partial\Omega_{\text{gl}}^{\text{pz}}$, and $\partial\Omega_{\text{gl}}^{\text{pm}}$.

Finally, the potential boundary condition (8a) is specified by the antisymmetric form around the $y = 0$ line of the voltages applied to each of the three electrodes of the 2D device, the top-left, top-right, and bottom electrodes,

$$\varphi_1 = +\frac{1}{2}\varphi_0, \quad \text{for } \mathbf{r} \in \partial\Omega_{\text{top-left}}^{\text{pz}}, \quad (42a)$$

$$\varphi_1 = -\frac{1}{2}\varphi_0, \quad \text{for } \mathbf{r} \in \partial\Omega_{\text{top-right}}^{\text{pz}}, \quad (42b)$$

$$\varphi_1 = 0, \quad \text{for } \mathbf{r} \in \partial\Omega_{\text{bottom}}^{\text{pz}}. \quad (42c)$$

VI. NUMERICAL IMPLEMENTATION IN COMSOL MULTIPHYSICS

Following the previous work from our group, the governing partial differential equations (PDEs) are implemented in the finite-element method software COMSOL Multiphysics [42] using the “Weak Form PDE Interface” [31,35] (see a sample script in the supplemental material of Ref. [43]). All simulations consist of two study steps: In step 1, the first-order acoustic equations are solved, and the result is passed on to step 2, in which the time-averaged second-order equations are solved using the first-order solutions in the different source terms.

In the Full model, the acoustic fields are the pressure p_1 and the full acoustic velocity \mathbf{v}_1 in the fluid, the displacement \mathbf{u}_1 in the solids, and the electric potential φ_1 in the transducer. The governing equations of these fields are Eqs. (4), (7), and (15), and the corresponding boundary conditions are Eqs. (6), (8), and (42). The time-averaged fields are only the pressure p_2 and the full streaming field \mathbf{v}_2 in the fluid, with the governing Stokes-flow equation and Stokes-drift boundary condition both given in Eqs. (24).

In the BL25 model, the acoustic field is just the pressure p_1 in the fluid, the displacement \mathbf{u}_1 in the solids, and

the electric potential φ_1 in the transducer. The governing equations of these fields are Eqs. (4), (7), and (17c), and the corresponding boundary conditions are Eqs. (6) and (8) as well as the self-consistent effective boundary-layer conditions for the pressure and the stress, Eqs. (22) and (23). The time-averaged fields are only the excess pressure \tilde{p}_2^d and the long-range bulk streaming field \mathbf{v}_2^d in the fluid, with the governing weakly compressional Stokes-flow equation (37) and the effective boundary-layer velocity slip condition given by Eqs. (39) in combination with Eqs. (35) and (38).

An important technical note regards third derivatives in COMSOL, which appear several places in the boundary conditions (35), such as $\partial_z \partial_y v_{1x}^d \propto \partial_z \partial_y \partial_x p_1$. In COMSOL, such a term is set to zero, as three consecutive derivatives of any field are not allowed. Consequently, we introduce an auxiliary vector field \mathbf{G}_1 equal to the pressure gradient ∇p_1 such that its k th component is $G_{1k} = \partial_k p_1$. Following Eq. (17a), we set $\mathbf{v}_1^d = -[i(1 - i\Gamma)/\omega\rho_0]\mathbf{G}_1$, which in COMSOL has nonzero second derivatives, such as $\partial_z \partial_y v_{1x}^d \neq 0$.

To understand the following details in the COMSOL implementation, it is relevant to mention that in COMSOL the partial x derivative $\partial_x f$ of a scalar field f is written by appending a lower-case “x” to “f” as “fx”. Thus the Cartesian coordinates of the gradient ∇f are written as “(fx, fy, fz)”. To avoid ambiguities, the Cartesian vector components of a vector \mathbf{v} are represented by upper-case letters such as “(vX, vY, vZ)”. The partial x derivative $\partial_x v_x$ of the component v_x is thus written “vXx”.

In the COMSOL implementation of the effective boundary conditions of the BL25 model, the local tangential and normal unit vectors $\mathbf{e}_\xi = \mathbf{t}_1$, $\mathbf{e}_\eta = \mathbf{t}_2$, and $\mathbf{e}_\zeta = \mathbf{n}$, the tangential derivatives ∇_{\parallel} , and the time average $\langle a_1, b_1 \rangle$ of first-order products $a_1 b_1$ play a crucial role. In COMSOL, the local tangential and normal vectors have the Cartesian components “(t1X, t1Y, t1Z)”, “(t2X, t2Y, t2Z)”, and “(nX, nY, nZ)”, respectively. As we work only in the limit of weakly curved interfaces, as described in Sec. IID, all ζ derivatives of normal and tangential vectors are neglected. For example, the ζ derivative $\partial_\zeta v_\zeta$ of the ζ component of the interface vector \mathbf{v}^0 is computed as $\partial_\zeta (\mathbf{n} \cdot \mathbf{v}^0) \approx \mathbf{n} \cdot \partial_\zeta \mathbf{v}^0 = n_i (n_k \partial_k) v_i^0$, which in COMSOL is the nine-term sum “nX*nX*vXx + nX*nY*vXy + . . . + nZ*nZ*vZz”. The tangential derivatives are computed without approximations using the COMSOL operator “dtang()”, and the time averages are computed using the COMSOL operator “realdot()”. To avoid the spurious imaginary parts that sometimes appear, we explicitly take the real part, “real(realdot())” of all “realdot()” terms.

Since we cannot use δ as a superscript in COMSOL scripts, we introduce the superscript changes: $\delta \rightarrow$ “d” (for delta), $d \rightarrow$ “f” (for fluid bulk), and sl \rightarrow “s” (for solid). In COMSOL at the fluid-solid interface $\zeta = 0$, the Cartesian coordinates of the wall velocity \mathbf{V}_1^0 , the bulk fluid

velocity v_1^d , and the boundary-layer velocity v_1^s are written as “(vs1X, vs1Y, vs1Z)”, “(vf1X, vf1Y, vf1Z)”, and “(vd1X, vd1Y, vd1Z)”, where the latter according to $v_1^{\delta 0} = \mathbf{V}_1^0 - \mathbf{v}_1^{d0}$ is computed as “(vs1X-vf1X, vs1Y-vf1Y, vs1Z-vf1Z)”. As mentioned above, \mathbf{G}_1 is introduced as an auxiliary field equal to ∇p_1 by the weak-form definition “test (GK) * (GK-plk)” for $K = X, Y, Z$ and $k = x, y, z$. The bulk velocity and its gradient are correspondingly defined as “vf1K = (1-i*Gam0)/(i*omega*rho0)*GK” and “vf1Kn = (1-i*Gam0)/(i*omega*rho0)*GKn” with $K, N = X, Y, Z$ and $n = x, y, z$. All tangential derivatives after coordinate k of component K of the wall velocity \mathbf{V}_1^0 are computed as “vs1Ktk = dtang(vs1K, k)” with $K = X, Y, Z$ and $k = x, y, z$, and similar for v_1^{d0} and $v_1^{\delta 0}$. Here, “Ktk” in the name “vs1Ktk” is read as “the K th component’s tangential k derivative”.

Using this notation, we implement all the governing equations and boundary conditions of the BL25 model. In the following we show how the first-order boundary conditions are implemented, and then refer to Appendix C for a more detailed description including the elaborate second-order boundary conditions. The first-order pressure boundary condition (22) is written as “i*omega*rho0/(1-i*Gam0)*(nX*vs1X+nY*vs1Y+nZ*vs1Z - ii/ks*divparvs10) - ii/ks*(kc^2*p1 + plzetazeta)”, where “divparvs10” is the tangential divergence $\nabla_{\parallel} \cdot \mathbf{V}_{1\parallel}^0$ written as “vs1XtX+vs1YtY+vs1ZtZ” and “plzetazeta” is the second-order ζ derivative $\partial_{\zeta}^2 p_1 = (\mathbf{n} \cdot \nabla)(\mathbf{n} \cdot \nabla)p_1$ written as “= nX*nX*p1xx + 2*nX*nY*p1xy + 2*nX*nZ*p1xz + nY*nY*p1yy + 2*nY*nZ*p1yz + nZ*nZ*p1zz”. Similarly, the k component $\mathbf{e}_k \cdot \sigma_1^{\text{sl}} \cdot \mathbf{e}_{\zeta}$ of the first-order stress boundary condition (23) is written as “-p1*nK + i*ks*eta0*(vd1K+nK*vd1zeta)”, where $K = X, Y, Z$ and “vd1zeta = vd1X*nX+vd1Y*nY+vd1Z*nZ”.

VII. NUMERICAL VALIDATION

To validate the BL25 model numerically, we have simulated the 3D and 2D polymer-based acoustofluidic devices with elliptical fluid channels shown in Fig. 1 and with the material parameters tabulated in Table II. As described below, the BL25 model results were successfully first tested for internal consistency by performing a mesh-convergence test, and then they were compared with results obtained by direct numerical simulations of the same devices using the Full model. In 3D, we find that using the Full model for direct numerical simulation of acoustofluidic devices of typical experiments [10,48] is out of the question, as it would require more than 1000 GB of memory, making it harder to simulate even using the DTU High Performance Computing (HPC) cluster at our disposal. Hence, we consider the tiny, yet physically realistic,

device described above, which, although not of practical use, at least allows us to compare the BL25 model solutions with the Full model solutions. We remark that, even with this tiny device, we are close to the limit of the finest mesh resolution that we can obtain when running the Full model on the DTU HPC cluster. In the 2D case, we are not near this mesh resolution limit, and we compared both the BL25 and the BL18 model to the Full model.

Qualitative validation in the form of plots for selected field components g are supplemented by the quantitative relative deviation $\epsilon_2(g^B, g^F)$ of the BL model field g^B from the Full model field g^F using the L^2 -norm on the domain Ω [22],

$$\epsilon_2(g^B, g^F) = \frac{\|g^B - g^F\|_2}{\|g^F\|_2}, \quad \text{with } \|g\|_2 = \sqrt{\int_{\Omega} |g|^2 dV}. \quad (43)$$

A short summary of the following validation results is that the BL25 model can predict the Full model results accurately for first- and second-order fields in 3D and 2D, on and off resonance, and for hard glass-silicon and soft polymer devices. In contrast, the BL18 model (only tested in 2D) proved accurate only for first- and second-order fields in hard glass-silicon devices run on resonance.

A. Mesh convergence and computational times in 2D and 3D of the BL25 and Full model

We have performed a mesh-convergence study for both the 3D and 2D models to determine the mesh that gives a sufficient resolution for finding correctly converged solutions; see the details in Appendix D. The mesh size is quantified by a mesh scale s with $0.05 < s < 0.85$. When s is increased, more and smaller mesh elements are introduced, and a better-resolved mesh results. For a given field component g , we make a semilogarithmic plot $\epsilon_2(g_s, g_{0.85})$ versus s of the relative deviation $\epsilon_2(g_s, g_{0.85})$ of the solution g_s with mesh scale s from the solution $g_{0.85}$ with the maximum mesh scale $s = 0.85$ (the finest mesh). For all fields [in first order $p_1, v_{1,i}$ with $i = x, y, z$), $u_{1,i}$ with $i = x, y, z$), and φ_1 ; and in second order p_2 , and $v_{2,i}$ with $i = x, y, z$], we find that $\epsilon_2(s)$ for $s \gtrsim 0.2$ is well described by an exponential decay, which indicates that convergence is obtained. In particular for $s = 0.7$, all relative deviations are small, $\epsilon_2(0.7) < 0.01$, and we therefore choose this value of s as our converged mesh. As in Ref. [22], the first-order fields converge faster than the second-order fields.

The computational time and memory requirement for the various simulations using the converged mesh scale $s = 0.7$ are as follows. In 2D, all simulations are done using COMSOL 6.2 on an HP-Z4 workstation with an Intel Xeon W-2295 processor CPU @ 3.00 GHz and 512 GB of random access memory (RAM). All 2D simulations use

TABLE II. Parameter values at 25 °C used in the numerical simulation of fluids (water, iodixanol-water, and glycerol-water), solids (PMMA, NOA 86H glue), and transducers (PZT Pz27 and $Al_{0.6}Sc_{0.4}N$). For the isotropic solids $C_{12} = C_{11} - 2C_{44}$, and for the transducers $C_{12} = C_{11} - 2C_{66}$.

Parameter	Symbol	Value	Unit
<i>Water</i> [24]			
Mass density	ρ^{fl}	997.05	kg m^{-3}
Speed of sound	c_{fl}	1496.7	m s^{-1}
Compressibility	κ_{fl}	447.7	TPa^{-1}
Dynamic viscosity	η_{fl}	0.89	mPa s
Bulk viscosity	η_{fl}^b	2.485	mPa s
<i>Iodixanol-water 16 vol % solution</i> [20,24]			
Mass density	ρ^{fl}	1050.0	kg m^{-3}
Speed of sound	c_{fl}	1482.3	m s^{-1}
Compressibility	κ_{fl}	433.4	TPa^{-1}
Dynamic viscosity	η_{fl}	1.474	mPa s
Bulk viscosity	η_{fl}^b	1.966	mPa s
<i>Glycerol-water 99 vol % solution</i> [20,44]			
Mass density	ρ^{fl}	1260.4	kg m^{-3}
Speed of sound	c_{fl}	1922.8	m s^{-1}
Compressibility	κ_{fl}	214.6	TPa^{-1}
Dynamic viscosity	η_{fl}	1.137	Pa s
Bulk viscosity	η_{fl}^b	0.790	Pa s
<i>PMMA</i> [39]			
Mass density	ρ^{sl}	1162	kg m^{-3}
Elastic modulus	C_{11}	$7.18 - i0.183$	GPa
Elastic modulus	C_{44}	$1.55 - i0.111$	GPa
<i>Glue layer (NOA 86H)</i> [39]			
Mass density	ρ^{sl}	1300	kg m^{-3}
Elastic modulus	C_{11}	$4.65 - i0.51$	GPa
Elastic modulus	C_{44}	$1.21 - i0.12$	GPa
<i>PZT Pz27 bulk transducer</i> [45]			
Mass density	ρ^{pz}	7700	kg m^{-3}
Elastic modulus	C_{11}	$124 - i0.601$	GPa
Elastic modulus	C_{12}	$77 - i0.442$	GPa
Elastic modulus	C_{13}	$80 - i0.091$	GPa
Elastic modulus	C_{33}	$119 - i0.538$	GPa
Elastic modulus	C_{44}	$20.4 - i0.486$	GPa
Coupling constant	e_{15}	11.0	C m^{-2}
Coupling constant	e_{31}	-5.2	C m^{-2}
Coupling constant	e_{33}	16.3	C m^{-2}
Electric permittivity	ϵ_{11}	$982 \epsilon_0$	F m^{-1}
Electric permittivity	ϵ_{33}	$804(1 - i0.003) \epsilon_0$	F m^{-1}
<i>$Al_{0.6}Sc_{0.4}N$ thin-film transducer</i> [41,46,47]			
Mass density	ρ^{pz}	3300	kg m^{-3}
Elastic modulus	C_{11}	$313.8 - i0.157$	GPa
Elastic modulus	C_{12}	$150 - i0.075$	GPa
Elastic modulus	C_{13}	$139.2 - i0.069$	GPa
Elastic modulus	C_{33}	$197.1 - i0.099$	GPa
Elastic modulus	C_{44}	$108.6 - i0.054$	GPa
Coupling constant	e_{15}	-0.317	C m^{-2}
Coupling constant	e_{31}	-2.653	C m^{-2}
Coupling constant	e_{33}	2.734	C m^{-2}
Electric permittivity	ϵ_{11}	$22.5(1 + i0.0005)\epsilon_0$	F m^{-1}
Electric permittivity	ϵ_{33}	$22.5(1 + i0.0005)\epsilon_0$	F m^{-1}

the same 2D mesh, which has 23 145 mesh elements with 12 712 mesh vertices, which for the Full model results in 543 107 degrees of freedom (DoF), a computational time of 48 s, and a memory usage of 16.8 GB RAM, and which for the BL25 model results in 363 915 DoF, a computational time of 30 s, and a memory usage of 14.8 GB RAM.

For the 3D simulations, despite the small-sized device geometry, the computational time and memory requirement of the Full model forced us to use the DTU HPC cluster. To obtain a fair comparison of the computational time requirement between the Full model and the BL25 model, we therefore also ran the latter on the DTU HPC cluster. In 3D, the Full model mesh has 101 839 mesh elements with 25 060 vertices, which results in 2 536 778 DoF, a computational time of 26 min 26 s, and a memory usage of 348 GB RAM. In contrast, the 3D mesh of the BL25 model has only 35 098 mesh elements with 6344 vertices, which results in 278 078 DoF, a computational time of 1 min 11 s, and a memory usage of 33 GB RAM. Here we clearly see the huge reduction in the computational requirements when going from the Full model to the BL25 model in 3D simulations. We end by noting that the much higher computational cost of the Full model is caused not only by the fine resolution needed in the thin boundary layer, which by construction is avoided in the BL25 model, but also because, to obtain the same accuracy, the Full model requires a finer mesh in the bulk than the BL25 model.

B. 3D numerical validation of BL25 versus Full model: The tiny PMMA device with an ellipsoidal cavity

We now turn to the numerical validation of the BL25 model by comparing it to the Full model. This is done on the tiny submillimeter PMMA-based ellipsoidal-cavity device actuated by a thin-film transducer described in Sec. V A. The comparison covers simulation of the first- and second-order fields mentioned in Sec. VII, and we remark that, to the best of our knowledge, the Full model simulations are the first of its kind carried out for a 3D acoustofluidic device.

The thin-film transducer is attached at the bottom of the device as shown in Fig. 1(a), and the device is actuated by applying an ac voltage with frequency f and amplitude $+\frac{1}{2}\varphi_0$ ($-\frac{1}{2}\varphi_0$) on the top left-half (right-half) of the split top electrode, $\varphi_0 = 1$ V, and by grounding the bottom electrode. Using the BL25 model, the resonance frequency for the PMMA device is obtained as the position $f_{\text{res}} = 2.03$ MHz of the maximum energy density $E_{\text{ac}}(f)$ in a frequency sweep from 0 to 2.5 MHz in steps of 5.0 kHz, and we find that $E_{\text{ac}}(f_{\text{res}}) = 0.06 \text{ J m}^{-3}$.

Then we compute the first- and second-order acoustic fields in both the BL25 and the Full model at f_{res} . The comparison of the first- and second-order fields in the two models are presented in Figs. 2(a1) and 2(b1),

respectively. The relative deviation between the models is $\epsilon_2^{1st} \lesssim 0.5\%$ and $\epsilon_2^{2nd} \lesssim 2\%$ for the first- and second-order fields, respectively, and both models find that, for example, the first-order acoustic pressure inside the fluid channel has the amplitude 21 kPa and the maximum solid displacement of the PMMA is 1.5 nm.

The second-order velocity (streaming) fields are notoriously difficult to compute. We obtained them in the BL25 model by computing v_2^d using Eqs. (36) along with the slip boundary conditions (39), and in the Full model we solved the second-order Eqs. (24) to obtain the streaming fields also inside the numerically resolved boundary layers. The contour plots of the streaming velocity v_2 for the 3D tiny PMMA device obtained in the two models are shown in Figs. 2(a2) and 2(b2), respectively. We obtained the same streaming pattern in the two models in the bulk of the fluid volume, including the conventional Rayleigh streaming pattern with the four streaming rolls in the y - z plane, as well as the streaming pattern in the central x - y plane and x - z plane. In the plots we have normalized the streaming fields by the amplitude $v_{str} = \frac{3}{8}v_1^2/c_0 = 0.06 \mu\text{m s}^{-1}$ of the conventional Rayleigh streaming.

The good agreement between the BL25 and Full models is further corroborated by plotting the respective streaming velocity components along the two lines passing through the point $(0.1L_f, 0.1W_f, 0.5H_f)$ parallel to the y and z axis, respectively. The resulting line graphs are plotted in Figs. 2(c) and 2(d), where minor deviations can be seen closer to the boundary layers, which can be attributed to the coarser mesh used in the Full model. Since we are at the limit of the computational capability for using the Full model, the boundary layer in this model was not fully resolved, but nevertheless the relative deviation in terms of L^2 -norms for the line plots were $\epsilon_2 \leq 1.7\%$.

C. 2D numerical validation of BL25 versus Full model: Normal-sized PMMA device with an elliptic cavity

As the final part of the numerical validation of the BL25 model, we consider the 2D cross section of the normal-sized long, straight PMMA device with an elliptic water-filled microchannel, which was introduced in Fig. 1(b) together with the parameter lists in Tables I and II. Like conventional acoustofluidic devices, the 2D PMMA device is actuated by a bulk-sized piezoelectric transducer glued by a thin layer of glue to the bottom surface of the PMMA block. Going to 2D has the advantage that the problems related to the extensive computer memory requirements in 3D are avoided, and we can also redo the numerical validation of the BL18 model, which was done only in 2D in the original work [31]. For better comparison, we have used the same mesh in Full and BL models in the present analysis, although a coarser mesh would suffice for the BL models [31].

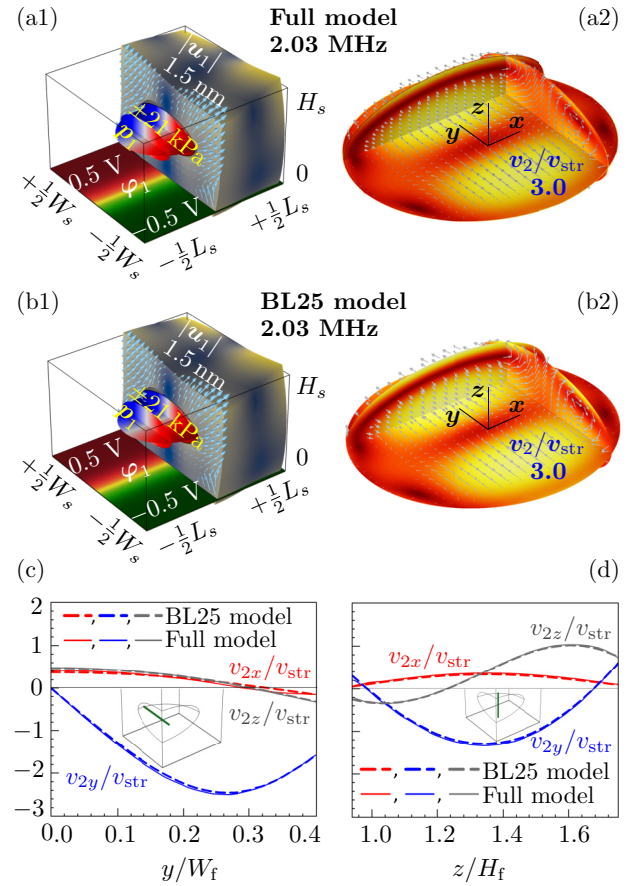


FIG. 2. Validating the first- and second-order fields of the BL25 model against the Full model for the tiny submillimeter 3D PMMA device actuated by a piezoelectric split-top-electrode thin-film transducer at the resonance frequency $f_{res} = 2.03$ MHz; see Fig. 1(a) and Table I. (a1) Color plot of the Full model first-order pressure p_1 from -21 kPa (blue) to $+21$ kPa (red), the amplitude of the displacement field $|u_1|$ from 0 (dark blue) to 1.5 nm (yellow), and the electrical potential ϕ_1 from -0.5 V (green) to $+0.5$ V (red). (a2) Vector plot of the Full model streaming velocity v_2 and color plot of its normalized magnitude v_2/v_{str} from 0 (dark red) to 3.0 (light yellow). (b1) Same as panel (a1), but for the BL25 model. (b2) Same as panel (a2), but for the BL25 model. (c) Comparison of line plots of the streaming field components for the Full and BL25 models along the green line parallel to the y direction. (d) Same as panel (c), but plotting along the green line parallel to the z axis.

Similar to the 3D device, the transducer of the 2D has a split top electrode, and it is actuated by applying an ac voltage with frequency f and amplitude $+\frac{1}{2}\varphi_0$ ($-\frac{1}{2}\varphi_0$) on the top left-half (right-half) of the split top electrode, $\varphi_0 = 1$ V, and by grounding the bottom electrode. As in 3D, the resonance frequencies f_{res} of the 2D PMMA device are obtained as those leading to local maxima $E_{ac}(f_{res})$ when computing the acoustic energy density E_{ac} versus frequency from 0.5 to 2.5 MHz in steps of 5 kHz. The relevant resonance frequency here is $f_{res} = 0.98$ MHz, which

clearly, and in accordance with the WSUR principle for acoustically soft (PMMA) devices [21], is much lower than the corresponding resonance mode (~ 2 MHz) in an acoustically hard (glass) device.

In Figs. 3(a1), 3(b1), and 3(c1) are shown the simulated contour plots of the first-order fields for the 2D PMMA device at resonance, $f_{\text{res}} = 0.98$ MHz, obtained from the Full model, the BL25 model, and the BL18 model, respectively. The resonance mode here is a mixed-mode type with two pressure nodal lines (planes in 3D) parallel to the y and z directions. The amplitude of the first-order acoustic pressure p_1 inside the channel is found to be 12.4 kPa, and the maximum displacement u_1 of the PMMA is 12.7 nm. All three models predict the same first-order fields, and the relative deviations from the Full model are small, $\epsilon_2^{\text{1st}} \lesssim 0.01$ for both the BL25 and the BL18 models.

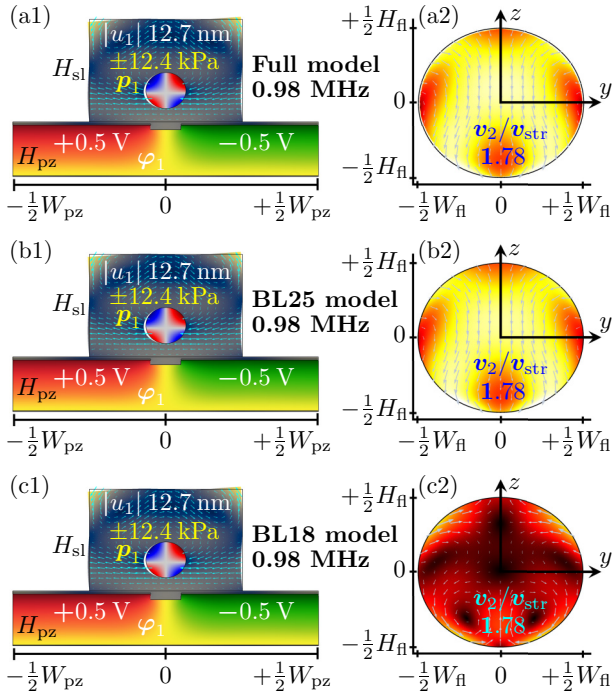


FIG. 3. Validating the first- and second-order fields in the BL25 and BL18 models against the Full model for the millimeter-sized 2D PMMA device actuated by a piezoelectric split-top-electrode bulk transducer at the resonance frequency $f_{\text{res}} = 0.98$ MHz; see Fig. 1(b) and Table I. (a1) Full model first-order fields: pressure field p_1 from -12.4 kPa (blue) to $+12.4$ kPa (red), the magnitude of solid displacement field $|u_1|$ from 0 (dark blue) to 12.4 nm (yellow), the first-order electrical potential from -0.5 V (green) to $+0.5$ V (red) via the grounded electrode value of 0 V (yellow). (a2) Full model second-order streaming field normalized with the Rayleigh streaming velocity from 0 (dark red) to 1.78 (yellow). (b1) Similar to panel (a1), but for the BL25 model. (b2) Similar to panel (a2), but for the BL25 model. (c1) Similar to panel (a1), but for the BL18 model. (c2) Similar to panel (a2), but for the BL18 model.

In Figs. 3(a2), 3(b2), and 3(c2) are shown the simulated contour plots of the second-order streaming field for the 2D PMMA device at resonance, $f_{\text{res}} = 0.98$ MHz, obtained from the Full model, the BL25 model, and the BL18 model, respectively. Whereas the BL25 model still has a small relative deviation from the Full model, $\epsilon_2(v_2^{\text{BL25}}, v_2^{\text{FM}}) = 2\%$, the BL18 model fails completely both quantitatively with $\epsilon_2(v_2^{\text{BL18}}, v_2^{\text{FM}}) = 96\%$ and predicting a qualitatively wrong solution. We note that when computing the L^2 -norm we exclude the region closer than $15 \mu\text{m}$ to avoid the boundary layers where the BL models by construction deviate from the Full model. In this mixed-mode resonance, the conventional Rayleigh streaming pattern with four flow rolls does not appear, but for convenience we still plot the streaming fields normalized with the Rayleigh streaming velocity $v_{\text{str}} = \frac{3}{8}v_1^2/c_0 = 0.06 \mu\text{m s}^{-1}$. This comparison highlights the necessity of replacing the BL18 model by the BL25 model.

To further study the extent to which the BL25 and BL18 models reproduce the Full model results for the second-order streaming velocity, we supplement the current elliptical channel cross section with eccentricity 0.44 by another with eccentricity 0.87, both embedded in PMMA (soft) and in glass (hard). The respective relative deviations ϵ_2 from the Full model are listed in Table III.

Clearly, the BL25 model is more accurate than the BL18 model. The relative deviation of the BL25 model from the Full model is at most 4%, whereas the BL18 model deviates typically by 10% or more. However, we note that the BL18 model is performing better for the hard glass devices than for the soft PMMA devices, and the best performance of the BL18 model is at resonance frequencies in hard devices, exactly the case that was tested previously [31,35]. The reason for this behavior is that the

TABLE III. The relative deviation $\epsilon_2(v_2^B, v_2^F)$ of the BL25 and BL18 models from the Full model simulation of the acoustic streaming v_2 for elliptic channels with eccentricity $e = 0.44$ [Fig. 1(b)] and $e = 0.87$, embedded in (soft) PMMA and in (hard) glass, and actuated at the frequency f . Boldfaced entries are computed at resonance.

f (MHz)	2D device with PMMA		2D device with glass	
	$\epsilon_2(v_2^{25}, v_2^F)$	$\epsilon_2(v_2^{18}, v_2^F)$	$\epsilon_2(v_2^{25}, v_2^F)$	$\epsilon_2(v_2^{18}, v_2^F)$
<i>Elliptical channel cross section with eccentricity $e = 0.44$</i>				
0.98	4%	96%	3%	16%
1.52	2%	13%	1%	27%
3.66	3%	24%	1%	7%
4.02	1%	14%	1%	9%
<i>Elliptical channel cross section with eccentricity $e = 0.87$</i>				
0.98	3%	148%	3%	20%
1.97	1%	25%	1%	2%
3.95	1%	13%	2%	36%
4.27	1%	18%	2%	16%

prefactors of the terms in the higher orders of $k\delta$ previously neglected are so large that these terms cannot be neglected. The inclusion of these terms is exactly what distinguishes the BL25 model from the BL18 model, and we now see the result: the BL25 model is accurate both on and off resonance for both hard and soft devices. It is worth mentioning that the computation time of the complex and more accurate BL25 model is not significantly different from the simpler BL18 model. The reason is that the model complexity only affects the short time for initializing the finite-element matrix, but not the subsequent long time spent by the finite-element solver.

So far, we have discussed only geometries without sharp corners. However, the right angles in a rectangular channel cross section are sharp with zero curvature. Thus, this common geometry breaks the fundamental assumption of weak curvature, on which the boundary-layer models are founded. To investigate corner effects, we have simulated 2D rectangular devices, and the results are presented in the Supplemental Material [37]. In summary, we found that in (hard) glass devices on resonance, the relative deviations are small for both BL25 and BL18, $\epsilon_2(v_2^{25}, v_2^F) = 0.4\%$ and $\epsilon_2(v_2^{18}, v_2^F) = 2\%$, but for the (soft) PMMA

device, only BL25 remains accurate whereas BL18 fails, $\epsilon_2(v_2^{25}, v_2^F) = 4\%$ and $\epsilon_2(v_2^{18}, v_2^F) = 78\%$. So, also regarding corner effects in rectangular channels, the replacement of the BL18 model by the BL25 model is necessary for accurate simulations.

VIII. MODEL COMPARISON WITH EXPERIMENTAL DATA

Lastly, for an experimental validation of the BL25 model, we revisit the PMMA device [see Fig. 4(a) and Table IV] fabricated and tested by Lickert *et al.* [20] to demonstrate by experiments and by numerical BL18 simulations that (soft) polymer-based acoustofluidic devices can perform acoustophoretic particle focusing. We show below that using the BL25 model together with updated values of the acoustic parameters of PMMA, we are able to predict quantitatively the measured resonance frequency f_{res} within 1%, and both the electrical admittance Y and the acoustic energy density E_{ac} within 15%. These results are an improvement of the BL18 model simulations of Ref. [20], which predicted the measured f_{res} with only

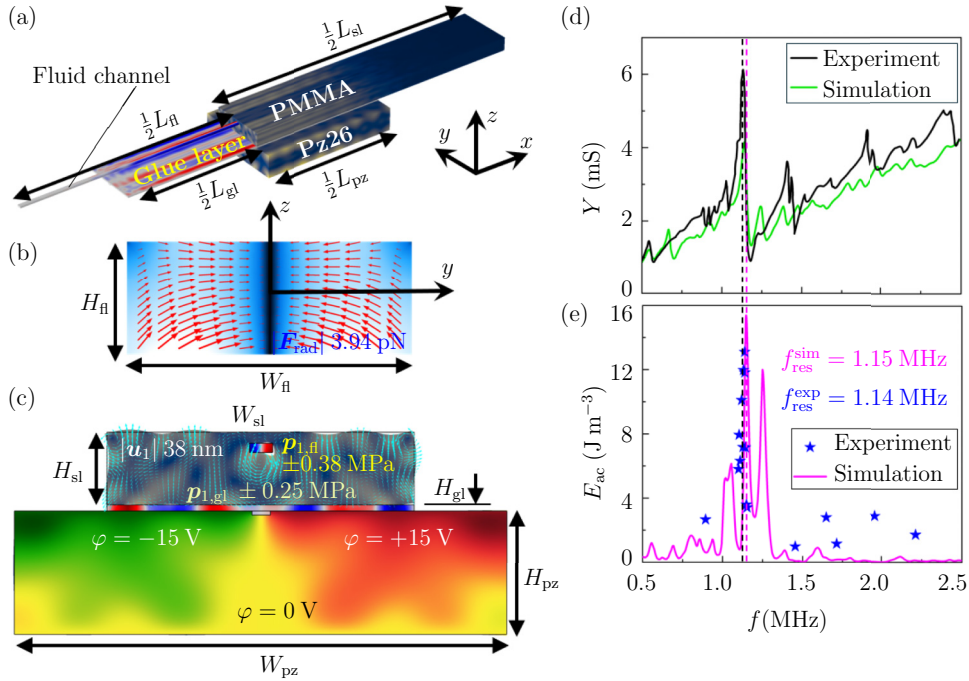


FIG. 4. BL25 model simulations in 3D of the PMMA device studied by Lickert *et al.* [20] with the parameters listed in Tables II, IV, and V. (a) Simulated first-order fields in 3D at the resonance frequency $f_{\text{res}} = 1.15$ MHz: the pressure inside the fluid channel [$p_{1,\text{fl}}$ from -0.38 MPa (blue) to $+0.38$ MPa (red)] and inside the glue layer [$p_{1,\text{gl}}$ from -0.25 MPa (blue) to $+0.25$ MPa (red)]. (b) A vector plot (red) of the simulated acoustic radiation force \mathbf{F}^{rad} and a color plot of its magnitude $|\mathbf{F}^{\text{rad}}|$ from 0 (black) to 3.94 pN (white) in the y - z plane at $x = 0$. (c) Color and vector plots of the simulated first-order fields p_1 (both channel and coupling layer), \mathbf{u}_1 , and φ_1 in the cross section in the y - z plane at $x = 0$. (d) The measured (black) and the simulated (green) electrical admittance Y plotted versus frequency f exhibiting a strong resonance near $f = 1.15$ MHz. (e) Measured (stars) and simulated (line) acoustic energy density E_{ac} plotted versus frequency f . The measured and simulated resonance frequency f_{res} and corresponding $E_{\text{ac}}(f_{\text{res}})$ are found to be $f_{\text{res}}^{\text{exp}} = 1.14$ MHz with $E_{\text{ac}}^{\text{exp}} = 13$ J m $^{-3}$ and $f_{\text{res}}^{\text{sim}} = 1.15$ MHz with $E_{\text{ac}}^{\text{sim}} = 15$ J m $^{-3}$, respectively.

TABLE IV. The geometry parameters (Param.) and their values for the PMMA-based acoustofluidic device of Ref. [20] used in the present BL25 model simulation of the device.

Param.	Value	Param.	Value	Param.	Value
L_{pz}	24 mm	W_{pz}	8 mm	H_{pz}	2 mm
L_{sl}	50 mm	W_{sl}	5 mm	H_{sl}	1.18 mm
		H_{gl}	100 μm	$H_{\text{sl}}^{\text{hd}}$	0.18 mm
L_{gr}	24 mm	W_{gr}	300 μm	H_{gr}	65 μm
L_{fl}	40 mm	W_{fl}	375 μm	H_{fl}	150 μm

quantitative accuracy, while Y and E_{ac} were predicted merely qualitatively.

The current experimental validation of the BL25 model was carried out in a seven-step procedure:

(1) The acoustic parameters of the PMMA and the PZT transducer model Pz26 from CTS Ferroperm [49] were determined using our in-house ultrasound electrical induced spectroscopy (UEIS) method [39]. This contrasts with the use of average literature values used in Ref. [20].

(2) The fluid properties for the iodixanol-water 16 vol% and glycerol-water 99 vol% solutions are set to the table values also used by Lickert *et al.* [20].

(3) The ill-determined thickness of the “glue” layer (here, the “glue” is actually the very viscous glycerol-water solution, but for simplicity still called “glue”) was initially set to 20 μm as in Ref. [20].

(4) The BL25 model was implemented in the water-filled channel where $\delta \approx 0.5 \mu\text{m}$, whereas the Full model was implemented in the highly viscous glycerol “glue” layer, where $\delta \approx 20 \mu\text{m}$ is so large that resolving the boundary layer numerically is unproblematic.

(5) The simulation was then executed. The solid and fluid domains were discretized with tetrahedral mesh elements of maximum size $h_{\text{solid}}^{\text{max}} = 375 \mu\text{m}$ and $h_{\text{fluid}}^{\text{max}} = 93.75 \mu\text{m}$, respectively, resulting in a mesh with 88 313 mesh elements, 13 670 boundary elements, and 1711 edge elements, and the total DoF being 1 546 206.

(6) We found that the glue-layer thickness plays a crucial role in damping the acoustic energy density in the fluid channel. Glycerol was used in the experiment to allow for easy mounting and dismounting of the device, but uniformity of the “glue” layer thickness is difficult to control experimentally. Its thickness was not measured in the experiment, but merely assumed to lie in the range from 20 to 100 μm . A study of the effects of the glue-layer thickness on the acoustic energy density of the fluid is presented in the Supplemental Material [37]. There we conclude that a thickness of $H_{\text{gl}} = 100 \mu\text{m}$ best fitted the experimental value of Y .

(7) With $H_{\text{gl}} = 100 \mu\text{m}$, we ran the BL25 model as a function of frequency from 0.5 to 2.5 MHz, the same range as in Ref. [20].

The simulation results are shown in Fig. 4, including the first-order fields (pressure p_1 , displacement \mathbf{u}_1 , and electric potential φ_1), the acoustic radiation force in Eq. (18b) \mathbf{F}^{rad} , and notably the averaged acoustic energy density in Eq. (18a) E_{ac} in the fluid, and the electrical admittance spectrum $Y(f)$ of the transducer loaded with PMMA and the fluid channel. The Y value is computed as the current I flowing into the positive electrode surface Ω_+ over the voltage difference φ_0 between the positive and negative electrodes, which in terms of D_z of Eq. (A2) is

$$Y(f) = \frac{1}{\varphi_0} \int_{\Omega_+} \mathbf{J} \cdot (-\mathbf{n}) da = \frac{i\omega}{\varphi_0} \int_{\Omega_+} D_z da. \quad (44)$$

The electrical admittance spectrum is presented in Fig. 4(d). In the BL25 model simulation, the maximum admittance value $Y_{\text{max}}^{\text{sim}} = 4.4 \text{ mS}$ is obtained at the frequency $f_{\text{res}}^{\text{sim}} = 1.15 \text{ MHz}$, which defines the resonance frequency. This is in fair agreement with the measured value $Y_{\text{max}}^{\text{exp}} = 6.0 \text{ mS}$ obtained at $f_{\text{res}}^{\text{exp}} = 1.13 \text{ MHz}$. Also off resonance in the entire frequency range, the BL25 model predicts fairly well within 10%–30% the entire admittance spectrum.

These results are consistent with the acoustic energy spectrum, presented in Fig. 4(e), where, in the BL25 model, the simulated maximum energy value $E_{\text{ac,max}}^{\text{sim}} = 15 \text{ J m}^{-3}$ is obtained at $f_{\text{res}}^{\text{sim}} = 1.15 \text{ MHz}$, the same frequency as for $Y_{\text{max}}^{\text{sim}}$, and the measured maximum energy value $E_{\text{ac,max}}^{\text{exp}} = 13 \text{ J m}^{-3}$ is obtained at $f_{\text{res}}^{\text{exp}} = 1.13 \text{ MHz}$, the same frequency as for $Y_{\text{max}}^{\text{exp}}$. Thus $E_{\text{ac,max}}^{\text{sim}}$ deviates only 15% from $E_{\text{ac,max}}^{\text{exp}}$, which is an improvement of the numerical model compared to the 550% deviation found in Ref. [20]. In short, we find that the BL25 model is validated against experimental data from the literature. The predicted resonance frequency deviates only 1% from the measured one, and the predicted admittance and acoustic energy density deviate around 15%.

We end this section by noting that we have observed that in the BL25 model the above fluid resonance frequency does not deviate from the resonance frequency of the unloaded Pz26 transducer, which in simulation and experiment was found to be $f_{\text{res}}^{\text{pz,sim}} = 1.145 \text{ MHz}$ and $f_{\text{res}}^{\text{pz,exp}} = 1.14 \text{ MHz}$, respectively, in contrast to the mismatch between the resonance frequency of the unloaded transducer and the fluid reported by Lickert *et al.* [20].

The BL25 model corroborates the ability of the soft PMMA device to perform particle focusing. In Fig. 4(c) is shown how, for an applied voltage of 30 V_{pp} , a strong displacement (28 nm) of the PMMA occurs just below the fluid channel in a pattern that creates an antisymmetric wave that leads to the formation of a half standing wave inside the fluid channel with the pressure node aligned vertically along the fluid center of magnitude

0.38 MPa. For application purposes, the more interesting quantity to study is the acoustic radiation force acting on suspended microparticles in the fluid channel, as shown in Fig. 4(b) for 5- μm -diameter polystyrene particles as used in Ref. [20]. The maximum force obtained from the simulation is 3.9 pN in the bottom half of the microchannel, and it is seen how the horizontal component generally is larger than the vertical one. This is quantified by the figure of merit [21], defined as $R = \int_{V_{\text{fl}}} -\text{sign}(y)F_y^{\text{rad}} dV / \int_{V_{\text{fl}}} |F_z^{\text{rad}}| dV = 3.1$, a value comparable to those found in the ideal 2D cases studied in Ref. [21], and indicating an acoustophoretic ability of decent quality.

IX. SUMMARY AND CONCLUDING REMARKS

The core of the theory developed by Bach and Bruus [31] is the decomposition of the first- and second-order acoustic fields into short-range boundary-layer fields, which vary on the length scale δ , and long-range bulk fields, which vary on the length scale of the inverse of wave number k_0^{-1} . This decomposition enables an analytical evaluation of the boundary-layer field given the assumptions that the wall motion is small and the fluid-solid curvature is large. With these prerequisites, Bach and Bruus developed the BL18 model in terms of a slip velocity boundary condition for the streaming velocity field valid to lowest order in the small parameter $k_0\delta \approx 0.003$. Since the BL18 model avoids the need to resolve the thin boundary layer numerically, it enables simulation of actual acoustofluidic devices in 3D. So far, the BL18 model has been tested only for (hard) glass and glass-Si devices [31,35], but remarkably we have demonstrated in this work that, for soft polymer-based devices, the higher-order $k_0\delta$ terms, hitherto neglected in the BL18 model, must be included to obtain a quantitatively correct description of (soft) polymer acoustofluidic devices, even in cases where the BL18 model fails to predict qualitatively correct responses. We call this improved model the BL25 model.

In Sec. III B, the boundary condition derived for the first-order pressure p_1 in the BL25 model is identical to that of the BL18 model. However, in Sec. III C, one extra term is added to the first-order stress boundary condition in the BL25 model compared to the BL18, the first difference between the two models.

Going to the second-order streaming field v_2 , the two models differ more substantially. We found that, for acoustically soft materials like polymers, it is important to include terms of one higher order in $k\delta$ than was done in the BL18 model, as the polymer wall velocity can be more than one order of magnitude larger than that of a hard glass or glass-Si device. In particular, the larger wall velocity facilitates a larger short-ranged perpendicular boundary-layer velocity component v_{2z}^{sl} , resulting in

the non-negligible influence of the higher-order terms in the short-range boundary-layer velocity v_2^{sl} , Eqs. (35).

The main theoretical result of this work is the final form of the slip boundary condition, Eq. (39), of the BL25 model, comprising a total of 25 terms for the long-range streaming field for v_2^{sl} , obtained by combining short-range velocity v_2^{sl} and the Stokes-drift velocity v_2^{sd} , Eqs. (35) and (38).

The main modeling result is the implementation of the BL25 model in the finite-element method using the “Weak Form PDE Interface” of the software COMSOL Multiphysics, described in Sec. VI. Here, the detailed implementation of the tangential and perpendicular derivatives on the weakly curved fluid-solid interface, which appears in the above-mentioned boundary conditions, is essential.

Finally, the main simulation results are the numerical and experimental validation of the BL25 model presented in Secs. VII and VIII based on the 3D and 2D models introduced in Sec. V and the experimental device described in Sec. VIII, all shown in Figs. 1 and 4, respectively. The first step in the numerical validation was the mesh-convergence study presented in Sec. VII A, which revealed satisfactory convergence of the first- and second-order fields in the BL25 model. In all cases, an asymptotic behavior approached exponentially was obtained for all fields as a function of refining the mesh.

The second numerical validation step was the comparison in 3D between the BL25 model and the Full model presented in Sec. VII B. This validation is not trivial, as the main point in developing the BL25 model is to be able to perform 3D device simulation. However, by introducing a tiny submillimeter model device, still containing all the essential components of an acoustofluidic device, we were able to simulate the acoustofluidic response in both models by stretching our available computer resources to the limit. To our knowledge, this may be the first example of a Full model simulation of an acoustofluidic device. This validation was successful, as we found the relative deviation between the models to be $\epsilon_2^{\text{1st}} \lesssim 0.5\%$ and $\epsilon_2^{\text{2nd}} \lesssim 2\%$ for the first- and second-order fields, respectively.

The third numerical validation step, presented in Sec. VII C, was to compare simulation results in 2D of both the BL25 model and the BL18 model to the Full model. The results are summarized in Fig. 3 and Table III. The BL25 model predicts the results of the Full model with both qualitative and quantitative accuracy, with relative deviations from the Full model being at most 4% in all shown cases, including both hard glass and soft PMMA devices being driven both on and off resonance. In contrast, the BL18 model only obtains the same good level of quantitative agreement with the Full model in the cases previously tested, hard devices run at resonance [31,35], whereas large quantitative deviations are seen for soft polymer devices both on and off resonance, and, somewhat surprisingly, also for hard glass devices run off resonance.

Importantly, we even found cases where the predictions of the BL25 model matched the Full model, whereas the BL18 model predicted qualitatively wrong responses, such as the example shown in Fig. 3(c2).

In a final 2D numerical validation, we found that, even in the case of devices with rectangular channel cross sections, where the four corners with their zero radius of curvature clearly violate the basic assumption of the BL25 and BL18 models that the curvature must be sufficiently large compared to the boundary-layer thickness δ , the BL25 model deviated very little from the Full model, whereas the BL18 model failed. Specifically, we found the relative deviations $\epsilon_2(v_2^{25}, v_2^F) = 4\%$ and $\epsilon_2(v_2^{18}, v_2^F) = 78\%$ in the (soft) PMMA device run at resonance. For a (hard) glass device at resonance, both models did better, with $\epsilon_2(v_2^{25}, v_2^F) = 0.4\%$ and $\epsilon_2(v_2^{18}, v_2^F) = 2\%$.

Finally, the experimental validation against published data in the literature by Lickert *et al.* [20] for a (soft) PMMA device driven by a PZT Pz26 transducer, presented in Sec. VIII, shows that the BL25 model can predict the measured resonance frequency within 1% and the measured electrical admittance of the loaded PZT Pz26 transducer as well as the acoustic energy density in the water-filled channel both qualitatively and quantitatively (within about 15%). In this validation, the thickness of the glycerol “glue” layer was the only fitting parameter. This is in contrast to the previous BL18 model results also published in Ref. [20], where the electrical admittance and the acoustic energy density deviated by nearly an order of magnitude from the experimental data. This experimental validation could be improved by knowing the specific clamping of the device in the sample holder and the actual thickness of the “glue” layer.

Given the extensive validation simulations showing that the BL25 model is in good quantitative agreement (within 4%) with the Full model for both first- and second-order fields and both on and off resonance, given the quantitative agreement (within 15%) with experimental data, and given that the BL25 model in all cases performs better than the previous BL18 model, it appears to be justified to introduce the complex BL25 model comprising the 25 terms in Eq. (39). It is worth mentioning that the computation time of the complex BL25 model is not significantly different from that of the simpler BL18 model.

The application range of the BL25 model goes beyond the few examples presented in this paper, which focused mainly on polymer-based devices driven at low megahertz frequencies, as long as the above-mentioned assumptions of the model are respected. For example, the BL25 model is ideally suited to contribute to the understanding of which types of streaming is dominating in a given device. The typical acoustofluidic device studied in this work has a fluid cavity with a 375- μm -wide ($= \frac{1}{2}\lambda$) and 200- μm -high ($< \frac{1}{2}\lambda$) cross section, actuated with a single standing half-wave resonance in the width direction. In this case the

Rayleigh streaming is always important, even in the center of the device. For a cross section with a height larger than the wavelength λ , the Rayleigh streaming extends of the order half a wavelength away from the walls in the height direction; thus in the center of such a device, the Rayleigh streaming may be negligible [22]. Conversely, the Eckart streaming is usually important in devices much longer than the attenuation length, which can be orders of magnitude longer than the wavelength. However, as discussed in Ref. [50], in the case of rotating acoustic fields, Eckart streaming may be important even in devices of dimensions of the order of the acoustic wavelength. In the BL25 model, these two types of streaming are explicitly addressed: the slip condition (39) corresponds to the Rayleigh (boundary layer) streaming, whereas the source term comprising the energy flux due to time-average acoustic intensity in Eqs. (37) results in the Eckart (bulk) streaming.

Other aspects of streaming where the BL25 model may be applied include, but are not limited to, studies of the suppression of streaming in shape-optimized acoustofluidic devices [51], Eckart-streaming-dominated gigahertz acoustofluidics [52], and nonlinear effects that may arise due to increased actuation power [6,52,53].

Based on the presented results, we believe that the BL25 model will be an important tool in future modeling of actual 3D acoustofluidic devices, both as a means to unravel the intricate physical nature of such devices, and as part of design optimization for technological applications of such devices.

ACKNOWLEDGMENTS

This work was supported by the ACOUSOME project funded by the European Innovation Council (EIC), HORIZON EIC 2022 TRANSITION, Grant No. 101099787.

DATA AVAILABILITY

The data that support the findings of this article are openly available [37].

APPENDIX A: THE CONSTITUTIVE EQUATIONS FOR THE PIEZOELECTRIC TRANSDUCERS

The constitutive equations for the three types of piezoelectric transducers used in this work all have the same form. In the Voigt notation, the six independent components σ_{1ik}^{pz} of the symmetric stress tensor σ_1^{pz} and $s_{1ik}^{\text{pz}} = \frac{1}{2}(\partial_i u_{1k} + \partial_k u_{1i})$ of the symmetric strain tensor s_1^{pz} are represented by the six-dimensional Voigt vectors σ_1^V and s_1^V , whose transposed forms are

$$[\sigma_1^V]^T = \{\sigma_{1xx}^{\text{pz}}, \sigma_{1yy}^{\text{pz}}, \sigma_{1zz}^{\text{pz}}, \sigma_{1yz}^{\text{pz}}, \sigma_{1xz}^{\text{pz}}, \sigma_{1xy}^{\text{pz}}\}, \quad (\text{A1a})$$

$$[s_1^V]^T = \{s_{1xx}^{\text{pz}}, s_{1yy}^{\text{pz}}, s_{1zz}^{\text{pz}}, 2s_{1yz}^{\text{pz}}, 2s_{1xz}^{\text{pz}}, 2s_{1xy}^{\text{pz}}\}. \quad (\text{A1b})$$

These mechanical fields are supplemented by the electrical potential φ_1 and its gradient, the electric field $\mathbf{E}_1 = -\nabla\varphi_1$, as well as the electric displacement field \mathbf{D}_1 . The Voigt

representation of the constitutive equations for the piezoelectric transducers in a 9×9 matrix equation relating σ_1^V and \mathbf{D}_1 to s_1^V and $-\nabla\varphi_1$ is as follows:

$$\begin{pmatrix} \sigma_1^V \\ \mathbf{D}_1 \end{pmatrix} = \mathbf{M} \cdot \begin{pmatrix} s_1^V \\ -\nabla\varphi_1 \end{pmatrix}, \quad (\text{A2})$$

$$\mathbf{M} = \begin{pmatrix} C_{11} & C_{12} & C_{13} & 0 & 0 & 0 & 0 & 0 & -e_{31} \\ C_{12} & C_{11} & C_{13} & 0 & 0 & 0 & 0 & 0 & -e_{31} \\ C_{13} & C_{13} & C_{33} & 0 & 0 & 0 & 0 & 0 & -e_{33} \\ \hline 0 & 0 & 0 & C_{44} & 0 & 0 & 0 & -e_{15} & 0 \\ 0 & 0 & 0 & 0 & C_{44} & 0 & -e_{15} & 0 & 0 \\ 0 & 0 & 0 & 0 & 0 & C_{66} & 0 & 0 & 0 \\ \hline 0 & 0 & 0 & 0 & e_{15} & 0 & \varepsilon_{11} & 0 & 0 \\ 0 & 0 & 0 & e_{15} & 0 & 0 & 0 & \varepsilon_{11} & 0 \\ e_{31} & e_{31} & e_{33} & 0 & 0 & 0 & 0 & 0 & \varepsilon_{33} \end{pmatrix}.$$

The parameter values of the piezoelectric transducers used in this work are given in Table II for $\text{Al}_{0.6}\text{Sc}_{0.4}\text{N}$ and PZT Pz27, and in Table V for PZT Pz26.

APPENDIX B: SECOND-ORDER BOUNDARY-LAYER FIELDS

In this appendix, we compute the second-order, time-averaged, boundary-layer field pressure p_2^δ and velocity \mathbf{v}_2^δ in the fluid, based on the first- and second-order expressions given in Secs. III and IV. Following Eqs. (28a), the velocity field is split in two components, $\mathbf{v}_2^{\delta 0} = \mathbf{v}_2^{\delta p} + \mathbf{v}_2^{\delta v}$, which are treated independently.

TABLE V. Parameters of the PZT transducer of type Pz26 [54] used in the numerical simulations of the experimental PMMA device [20] described in Sec. VIII.

Parameter	Symbol	Value	Unit
Mass density	ρ^{pz}	7700	kg m^{-3}
Elastic modulus	C_{11}	$168 - i3.36$	GPa
Elastic modulus	C_{12}	$110 - i2.20$	GPa
Elastic modulus	C_{13}	$99.9 - i2.00$	GPa
Elastic modulus	C_{33}	$123 - i2.46$	GPa
Elastic modulus	C_{44}	$30.1 - i0.60$	GPa
Coupling constant	e_{15}	$9.86 - i0.20$	C m^{-2}
Coupling constant	e_{31}	$-2.8 + i0.06$	C m^{-2}
Coupling constant	e_{33}	$14.7 - i0.29$	C m^{-2}
Electric permittivity	ε_{11}	$828(1 - i0.02)\varepsilon_0$	F m^{-1}
Electric permittivity	ε_{33}	$700(1 - i0.02)\varepsilon_0$	F m^{-1}

1. Computation of p_2^δ

To obtain the coordinate-separated form of the source term ∇p_2^δ in Eq. (28), we first take the divergence of Eq. (27a), neglect the $\nabla \cdot \mathbf{v}_2^\delta$ terms of order Γ , and finally use $\nabla^2 p_2^\delta \approx \partial_\zeta^2 p_2^\delta$, to arrive at

$$\partial_\zeta^2 p_2^\delta = -\rho_0 \nabla \cdot [\nabla \cdot \langle \mathbf{v}_1^\delta \mathbf{v}_1^\delta + \mathbf{v}_1^d \mathbf{v}_1^\delta + \mathbf{v}_1^\delta \mathbf{v}_1^d \rangle]. \quad (\text{B1})$$

Then the coordinate-separated form of this expression is obtained by using Eqs. (31d) and (32), and we arrive at the following 20-term expression for $\partial_\zeta^2 p_2^\delta$,

$$\begin{aligned} \partial_\zeta^2 p_2^\delta = & -\rho_0 \left\{ +\nabla_{\parallel} \cdot \left[\nabla_{\parallel} \cdot \langle I_{qq}^{(0)} \mathbf{v}_{1\parallel}^{\delta 0}, \mathbf{v}_{1\parallel}^{\delta 0} \rangle \right] + \langle I_{qq}^{(-2)} v_{1\zeta}^{\delta 0}, v_{1\zeta}^{\delta 0} \rangle \right. \\ & + \nabla_{\parallel} \cdot \left[\langle I_{qq}^{(-1)} \mathbf{v}_{1\parallel}^{\delta 0}, v_{1\zeta}^{\delta 0} \rangle + \langle I_{qq}^{(-1)} v_{1\zeta}^{\delta 0}, \mathbf{v}_{1\parallel}^{\delta 0} \rangle \right] \\ & + \nabla_{\parallel} \cdot \left[\nabla_{\parallel} \cdot \langle I_{1q}^{(0)} \mathbf{v}_{1\parallel}^{d0}, \mathbf{v}_{1\parallel}^{\delta 0} \rangle \right] + I_{1q}^{(-2)} (v_{1\zeta}^{d0} v_{1\zeta}^{\delta 0}) \\ & + \nabla_{\parallel} \cdot \left[\langle I_{1q}^{(-1)} \mathbf{v}_{1\parallel}^{d0}, v_{1\zeta}^{\delta 0} \rangle + \langle I_{1q}^{(-1)} v_{1\zeta}^{d0}, \mathbf{v}_{1\parallel}^{\delta 0} \rangle \right] \\ & + \nabla_{\parallel} \cdot \left[\nabla_{\parallel} \cdot \langle I_{\zeta q}^{(0)} \partial_\zeta \mathbf{v}_{1\parallel}^{d0}, \mathbf{v}_{1\parallel}^{\delta 0} \rangle \right] + \langle I_{\zeta q}^{(-2)} \partial_\zeta v_{1\zeta}^{d0}, v_{1\zeta}^{\delta 0} \rangle \\ & + \nabla_{\parallel} \cdot \left[\langle I_{\zeta q}^{(-1)} \partial_\zeta \mathbf{v}_{1\parallel}^{d0}, v_{1\zeta}^{\delta 0} \rangle + \langle I_{\zeta q}^{(-1)} \partial_\zeta v_{1\zeta}^{d0}, \mathbf{v}_{1\parallel}^{\delta 0} \rangle \right] \\ & + \nabla_{\parallel} \cdot \left[\nabla_{\parallel} \cdot \langle I_{q1}^{(0)} \mathbf{v}_{1\parallel}^{\delta 0}, \mathbf{v}_{1\parallel}^{d0} \rangle \right] + \langle I_{q1}^{(-2)} v_{1\zeta}^{\delta 0}, v_{1\zeta}^{d0} \rangle \\ & + \nabla_{\parallel} \cdot \left[\langle I_{q1}^{(-1)} \mathbf{v}_{1\parallel}^{\delta 0}, v_{1\zeta}^{d0} \rangle + \langle I_{q1}^{(-1)} v_{1\zeta}^{\delta 0}, \mathbf{v}_{1\parallel}^{d0} \rangle \right] \\ & + \nabla_{\parallel} \cdot \left[\nabla_{\parallel} \cdot \langle I_{q\zeta}^{(0)} \mathbf{v}_{1\parallel}^{\delta 0}, \partial_\zeta \mathbf{v}_{1\parallel}^{d0} \rangle \right] + \langle I_{q\zeta}^{(-2)} v_{1\zeta}^{\delta 0}, \partial_\zeta v_{1\zeta}^{d0} \rangle \\ & \left. + \nabla_{\parallel} \cdot \left[\langle I_{q\zeta}^{(-1)} \mathbf{v}_{1\parallel}^{\delta 0}, \partial_\zeta v_{1\zeta}^{d0} \rangle + \langle I_{q\zeta}^{(-1)} v_{1\zeta}^{\delta 0}, \partial_\zeta \mathbf{v}_{1\parallel}^{d0} \rangle \right] \right\}. \quad (\text{B2}) \end{aligned}$$

The short-range pressure p_2^δ is obtained from $\partial_\zeta^2 p_2^\delta$ by integrating twice with respect to ζ . This amounts to the trivial substitution of $I_{ab}^{(n)}$ in Eq. (B2) by $I_{ab}^{(n+2)}$,

$$\begin{aligned}
p_2^\delta = & -\rho_0 \left\{ +\nabla_{\parallel} \cdot \left[\nabla_{\parallel} \cdot \left\langle I_{qq}^{(2)} \mathbf{v}_{1\parallel}^{\delta 0}, \mathbf{v}_{1\parallel}^{\delta 0} \right\rangle \right] + \left\langle I_{qq}^{(0)} v_{1\zeta}^{\delta 0}, v_{1\zeta}^{\delta 0} \right\rangle \right. \\
& + \nabla_{\parallel} \cdot \left[\left\langle I_{qq}^{(1)} \mathbf{v}_{1\parallel}^{\delta 0}, v_{1\zeta}^{\delta 0} \right\rangle + \left\langle I_{qq}^{(1)} v_{1\zeta}^{\delta 0}, \mathbf{v}_{1\parallel}^{\delta 0} \right\rangle \right] \\
& + \nabla_{\parallel} \cdot \left[\nabla_{\parallel} \cdot \left\langle I_{1q}^{(2)} \mathbf{v}_{1\parallel}^{d0}, \mathbf{v}_{1\parallel}^{\delta 0} \right\rangle \right] + I_{1q}^{(0)} (v_{1\zeta}^{d0} v_{1\zeta}^{\delta 0}) \\
& + \nabla_{\parallel} \cdot \left[\left\langle I_{1q}^{(1)} \mathbf{v}_{1\parallel}^{d0}, v_{1\zeta}^{\delta 0} \right\rangle + \left\langle I_{1q}^{(1)} v_{1\zeta}^{d0}, \mathbf{v}_{1\parallel}^{\delta 0} \right\rangle \right] \\
& + \nabla_{\parallel} \cdot \left[\nabla_{\parallel} \cdot \left\langle I_{\zeta q}^{(2)} \partial_\zeta \mathbf{v}_{1\parallel}^{d0}, \mathbf{v}_{1\parallel}^{\delta 0} \right\rangle \right] + \left\langle I_{\zeta q}^{(0)} \partial_\zeta v_{1\zeta}^{d0}, v_{1\zeta}^{\delta 0} \right\rangle \\
& + \nabla_{\parallel} \cdot \left[\left\langle I_{\zeta q}^{(1)} \partial_\zeta \mathbf{v}_{1\parallel}^{d0}, v_{1\zeta}^{\delta 0} \right\rangle + \left\langle I_{\zeta q}^{(1)} \partial_\zeta v_{1\zeta}^{d0}, \mathbf{v}_{1\parallel}^{\delta 0} \right\rangle \right] \\
& + \nabla_{\parallel} \cdot \left[\nabla_{\parallel} \cdot \left\langle I_{q1}^{(2)} \mathbf{v}_{1\parallel}^{\delta 0}, \mathbf{v}_{1\parallel}^{d0} \right\rangle \right] + \left\langle I_{q1}^{(0)} v_{1\zeta}^{\delta 0}, v_{1\zeta}^{d0} \right\rangle \\
& + \nabla_{\parallel} \cdot \left[\left\langle I_{q1}^{(1)} \mathbf{v}_{1\parallel}^{\delta 0}, v_{1\zeta}^{d0} \right\rangle + \left\langle I_{q1}^{(1)} v_{1\zeta}^{\delta 0}, \mathbf{v}_{1\parallel}^{d0} \right\rangle \right] \\
& + \nabla_{\parallel} \cdot \left[\nabla_{\parallel} \cdot \left\langle I_{q\zeta}^{(2)} \mathbf{v}_{1\parallel}^{\delta 0}, \partial_\zeta \mathbf{v}_{1\parallel}^{d0} \right\rangle \right] + \left\langle I_{q\zeta}^{(0)} v_{1\zeta}^{\delta 0}, \partial_\zeta v_{1\zeta}^{d0} \right\rangle \\
& \left. + \nabla_{\parallel} \cdot \left[\left\langle I_{q\zeta}^{(1)} \mathbf{v}_{1\parallel}^{\delta 0}, \partial_\zeta v_{1\zeta}^{d0} \right\rangle + \left\langle I_{q\zeta}^{(1)} v_{1\zeta}^{\delta 0}, \partial_\zeta \mathbf{v}_{1\parallel}^{d0} \right\rangle \right] \right\}. \quad (\text{B3})
\end{aligned}$$

2. Computation of $\mathbf{v}_{2\parallel}^{\delta p}$

The parallel component $\mathbf{v}_{2\parallel}^{\delta p}$ and perpendicular component $\mathbf{v}_{2\perp}^{\delta p}$ of the boundary-layer velocity $\mathbf{v}_2^{\delta p}$ are obtained by integration of Eq. (28b),

$$\begin{aligned}
\partial_\zeta^2 \mathbf{v}_{2\parallel}^{\delta p} &= \nabla_{\parallel} \frac{p_2^\delta}{\eta_0} \\
\implies \mathbf{v}_{2\parallel}^{\delta p}(\zeta) &= \nabla_{\parallel} \int^\zeta \int^{\zeta'} \frac{p_2^\delta(\zeta'')}{\eta_0} d\zeta'' d\zeta', \quad (\text{B4a})
\end{aligned}$$

$$\partial_\zeta^2 v_{2\zeta}^{\delta p} = \partial_\zeta \frac{p_2^\delta}{\eta_0} \implies v_{2\zeta}^{\delta p}(\zeta) = \int^\zeta \frac{p_2^\delta(\zeta')}{\eta_0} d\zeta'. \quad (\text{B4b})$$

The computation of $\mathbf{v}_{2\parallel}^{\delta p}$ ($v_{2\zeta}^{\delta p}$) involves integration of p_2^δ twice (once) with respect of ζ , which according to Eq. (30b) amounts to increasing the superscript in all factors $I_{ab}^{(n)}$ by 2 (by 1). Inserting p_2^δ from Eq. (B3) into Eqs. (B4a) and (B4b) leads to

$$\begin{aligned}
\mathbf{v}_{2\parallel}^{\delta p} &= -\frac{1}{\nu_0} \nabla_{\parallel} \left\{ \right. \\
& \left. + \nabla_{\parallel} \cdot \left[\nabla_{\parallel} \cdot \left\langle I_{qq}^{(4)} \mathbf{v}_{1\parallel}^{\delta 0}, \mathbf{v}_{1\parallel}^{\delta 0} \right\rangle \right] + \left\langle I_{qq}^{(2)} v_{1\zeta}^{\delta 0}, v_{1\zeta}^{\delta 0} \right\rangle \right.
\end{aligned}$$

$$\begin{aligned}
& + \nabla_{\parallel} \cdot \left[\left\langle I_{qq}^{(3)} \mathbf{v}_{1\parallel}^{\delta 0}, v_{1\zeta}^{\delta 0} \right\rangle + \left\langle I_{qq}^{(3)} v_{1\zeta}^{\delta 0}, \mathbf{v}_{1\parallel}^{\delta 0} \right\rangle \right] \\
& + \nabla_{\parallel} \cdot \left[\nabla_{\parallel} \cdot \left\langle I_{1q}^{(4)} \mathbf{v}_{1\parallel}^{d0}, \mathbf{v}_{1\parallel}^{\delta 0} \right\rangle \right] + I_{1q}^{(2)} (v_{1\zeta}^{d0} v_{1\zeta}^{\delta 0}) \\
& + \nabla_{\parallel} \cdot \left[\left\langle I_{1q}^{(3)} \mathbf{v}_{1\parallel}^{d0}, v_{1\zeta}^{\delta 0} \right\rangle + \left\langle I_{1q}^{(3)} v_{1\zeta}^{d0}, \mathbf{v}_{1\parallel}^{\delta 0} \right\rangle \right] \\
& + \nabla_{\parallel} \cdot \left[\nabla_{\parallel} \cdot \left\langle I_{\zeta q}^{(4)} \partial_\zeta \mathbf{v}_{1\parallel}^{d0}, \mathbf{v}_{1\parallel}^{\delta 0} \right\rangle \right] + \left\langle I_{\zeta q}^{(2)} \partial_\zeta v_{1\zeta}^{d0}, v_{1\zeta}^{\delta 0} \right\rangle \\
& + \nabla_{\parallel} \cdot \left[\left\langle I_{\zeta q}^{(3)} \partial_\zeta \mathbf{v}_{1\parallel}^{d0}, v_{1\zeta}^{\delta 0} \right\rangle + \left\langle I_{\zeta q}^{(3)} \partial_\zeta v_{1\zeta}^{d0}, \mathbf{v}_{1\parallel}^{\delta 0} \right\rangle \right] \\
& + \nabla_{\parallel} \cdot \left[\nabla_{\parallel} \cdot \left\langle I_{q1}^{(4)} \mathbf{v}_{1\parallel}^{\delta 0}, \mathbf{v}_{1\parallel}^{d0} \right\rangle \right] + \left\langle I_{q1}^{(2)} v_{1\zeta}^{\delta 0}, v_{1\zeta}^{d0} \right\rangle \\
& + \nabla_{\parallel} \cdot \left[\left\langle I_{q1}^{(3)} \mathbf{v}_{1\parallel}^{\delta 0}, v_{1\zeta}^{d0} \right\rangle + \left\langle I_{q1}^{(3)} v_{1\zeta}^{\delta 0}, \mathbf{v}_{1\parallel}^{d0} \right\rangle \right] \\
& + \nabla_{\parallel} \cdot \left[\nabla_{\parallel} \cdot \left\langle I_{q\zeta}^{(4)} \mathbf{v}_{1\parallel}^{\delta 0}, \partial_\zeta \mathbf{v}_{1\parallel}^{d0} \right\rangle \right] + \left\langle I_{q\zeta}^{(2)} v_{1\zeta}^{\delta 0}, \partial_\zeta v_{1\zeta}^{d0} \right\rangle \\
& \left. + \nabla_{\parallel} \cdot \left[\left\langle I_{q\zeta}^{(3)} \mathbf{v}_{1\parallel}^{\delta 0}, \partial_\zeta \mathbf{v}_{1\parallel}^{d0} \right\rangle + \left\langle I_{q\zeta}^{(3)} v_{1\zeta}^{\delta 0}, \partial_\zeta \mathbf{v}_{1\parallel}^{d0} \right\rangle \right] \right\} \quad (\text{B5})
\end{aligned}$$

and

$$\begin{aligned}
v_{2\zeta}^{\delta p} &= -\frac{1}{\nu_0} \left\{ +\nabla_{\parallel} \cdot \left[\nabla_{\parallel} \cdot \left\langle I_{qq}^{(3)} \mathbf{v}_{1\parallel}^{\delta 0}, \mathbf{v}_{1\parallel}^{\delta 0} \right\rangle \right] + \left\langle I_{qq}^{(1)} v_{1\zeta}^{\delta 0}, v_{1\zeta}^{\delta 0} \right\rangle \right. \\
& + \nabla_{\parallel} \cdot \left[\left\langle I_{qq}^{(2)} \mathbf{v}_{1\parallel}^{\delta 0}, v_{1\zeta}^{\delta 0} \right\rangle + \left\langle I_{qq}^{(2)} v_{1\zeta}^{\delta 0}, \mathbf{v}_{1\parallel}^{\delta 0} \right\rangle \right] \\
& + \nabla_{\parallel} \cdot \left[\nabla_{\parallel} \cdot \left\langle I_{1q}^{(3)} \mathbf{v}_{1\parallel}^{d0}, \mathbf{v}_{1\parallel}^{\delta 0} \right\rangle \right] + \left\langle I_{1q}^{(1)} v_{1\zeta}^{d0}, v_{1\zeta}^{\delta 0} \right\rangle \\
& + \nabla_{\parallel} \cdot \left[\left\langle I_{1q}^{(2)} \mathbf{v}_{1\parallel}^{d0}, v_{1\zeta}^{\delta 0} \right\rangle + \left\langle I_{1q}^{(2)} v_{1\zeta}^{d0}, \mathbf{v}_{1\parallel}^{\delta 0} \right\rangle \right] \\
& + \nabla_{\parallel} \cdot \left[\nabla_{\parallel} \cdot \left\langle I_{\zeta q}^{(3)} \partial_\zeta \mathbf{v}_{1\parallel}^{d0}, \mathbf{v}_{1\parallel}^{\delta 0} \right\rangle \right] + \left\langle I_{\zeta q}^{(1)} \partial_\zeta v_{1\zeta}^{d0}, v_{1\zeta}^{\delta 0} \right\rangle \\
& + \nabla_{\parallel} \cdot \left[\left\langle I_{\zeta q}^{(2)} \partial_\zeta \mathbf{v}_{1\parallel}^{d0}, v_{1\zeta}^{\delta 0} \right\rangle + \left\langle I_{\zeta q}^{(2)} \partial_\zeta v_{1\zeta}^{d0}, \mathbf{v}_{1\parallel}^{\delta 0} \right\rangle \right] \\
& + \nabla_{\parallel} \cdot \left[\nabla_{\parallel} \cdot \left\langle I_{q1}^{(3)} \mathbf{v}_{1\parallel}^{\delta 0}, \mathbf{v}_{1\parallel}^{d0} \right\rangle \right] + \left\langle I_{q1}^{(1)} v_{1\zeta}^{\delta 0}, v_{1\zeta}^{d0} \right\rangle \\
& + \nabla_{\parallel} \cdot \left[\left\langle I_{q1}^{(2)} \mathbf{v}_{1\parallel}^{\delta 0}, v_{1\zeta}^{d0} \right\rangle + \left\langle I_{q1}^{(2)} v_{1\zeta}^{\delta 0}, \mathbf{v}_{1\parallel}^{d0} \right\rangle \right] \\
& + \nabla_{\parallel} \cdot \left[\nabla_{\parallel} \cdot \left\langle I_{q\zeta}^{(3)} \mathbf{v}_{1\parallel}^{\delta 0}, \partial_\zeta \mathbf{v}_{1\parallel}^{d0} \right\rangle \right] + \left\langle I_{q\zeta}^{(1)} v_{1\zeta}^{\delta 0}, \partial_\zeta v_{1\zeta}^{d0} \right\rangle \\
& \left. + \nabla_{\parallel} \cdot \left[\left\langle I_{q\zeta}^{(2)} \mathbf{v}_{1\parallel}^{\delta 0}, \partial_\zeta \mathbf{v}_{1\parallel}^{d0} \right\rangle + \left\langle I_{q\zeta}^{(2)} v_{1\zeta}^{\delta 0}, \partial_\zeta \mathbf{v}_{1\parallel}^{d0} \right\rangle \right] \right\}. \quad (\text{B6})
\end{aligned}$$

3. Computation of $\mathbf{v}_2^{\delta v}$

To determine $\mathbf{v}_2^{\delta v}$, we compute the coordinate-separated form of the source term in Eq. (28) by using Eqs. (31a) and (32),

$$\begin{aligned}
\partial_\zeta^2 \mathbf{v}_2^{\delta v} &= \frac{1}{\nu_0} \nabla \cdot \left\langle \mathbf{v}_1^\delta \mathbf{v}_1^\delta + \mathbf{v}_1^d \mathbf{v}_1^\delta + \mathbf{v}_1^\delta \mathbf{v}_1^d \right\rangle \\
&= \frac{1}{\nu_0} \left\{ \nabla_{\parallel} \cdot \left\langle I_{qq}^{(0)} \mathbf{v}_{1\parallel}^{\delta 0}, \mathbf{v}_{1\parallel}^{\delta 0} \right\rangle + \left\langle I_{qq}^{(-1)} \mathbf{v}_1^{\delta 0}, \mathbf{v}_{1\zeta}^{\delta 0} \right\rangle \right. \\
&\quad + \nabla_{\parallel} \cdot \left\langle I_{1q}^{(0)} \mathbf{v}_1^{d0}, \mathbf{v}_{1\parallel}^{\delta 0} \right\rangle + \left\langle I_{1q}^{(-1)} \mathbf{v}_1^{d0}, \mathbf{v}_{1\zeta}^{\delta 0} \right\rangle \\
&\quad + \nabla_{\parallel} \cdot \left\langle I_{\zeta q}^{(0)} \partial_\zeta \mathbf{v}_1^{d0}, \mathbf{v}_{1\parallel}^{\delta 0} \right\rangle + \left\langle I_{\zeta q}^{(-1)} \partial_\zeta \mathbf{v}_1^{d0}, \mathbf{v}_{1\zeta}^{\delta 0} \right\rangle \\
&\quad + \nabla_{\parallel} \cdot \left\langle I_{q1}^{(0)} \mathbf{v}_1^{\delta 0}, \mathbf{v}_{1\parallel}^{d0} \right\rangle + \left\langle I_{q1}^{(-1)} \mathbf{v}_1^{\delta 0}, \mathbf{v}_{1\zeta}^{d0} \right\rangle \\
&\quad \left. + \nabla_{\parallel} \cdot \left\langle I_{q\zeta}^{(0)} \mathbf{v}_1^{\delta 0}, \partial_\zeta \mathbf{v}_{1\parallel}^{d0} \right\rangle + \left\langle I_{q\zeta}^{(-1)} \mathbf{v}_1^{\delta 0}, \partial_\zeta \mathbf{v}_{1\zeta}^{d0} \right\rangle \right\}. \tag{B7}
\end{aligned}$$

From this, $\mathbf{v}_2^{\delta v}$ is found by integrating twice after ζ , which according to Eq. (30b) amounts to increase the superscript in all factors $I_{ab}^{(n)}$ by 2, which results in

$$\begin{aligned}
\mathbf{v}_2^{\delta v} &= \frac{1}{\nu_0} \left\{ \nabla_{\parallel} \cdot \left\langle I_{qq}^{(2)} \mathbf{v}_{1\parallel}^{\delta 0}, \mathbf{v}_{1\parallel}^{\delta 0} \right\rangle + \left\langle I_{qq}^{(1)} \mathbf{v}_1^{\delta 0}, \mathbf{v}_{1\zeta}^{\delta 0} \right\rangle \right. \\
&\quad + \nabla_{\parallel} \cdot \left\langle I_{1q}^{(2)} \mathbf{v}_1^{d0}, \mathbf{v}_{1\parallel}^{\delta 0} \right\rangle + \left\langle I_{1q}^{(1)} \mathbf{v}_1^{d0}, \mathbf{v}_{1\zeta}^{\delta 0} \right\rangle \\
&\quad + \nabla_{\parallel} \cdot \left\langle I_{\zeta q}^{(2)} \partial_\zeta \mathbf{v}_1^{d0}, \mathbf{v}_{1\parallel}^{\delta 0} \right\rangle + \left\langle I_{\zeta q}^{(1)} \partial_\zeta \mathbf{v}_1^{d0}, \mathbf{v}_{1\zeta}^{\delta 0} \right\rangle \\
&\quad + \nabla_{\parallel} \cdot \left\langle I_{q1}^{(2)} \mathbf{v}_1^{\delta 0}, \mathbf{v}_{1\parallel}^{d0} \right\rangle + \left\langle I_{q1}^{(1)} \mathbf{v}_1^{\delta 0}, \mathbf{v}_{1\zeta}^{d0} \right\rangle \\
&\quad \left. + \nabla_{\parallel} \cdot \left\langle I_{q\zeta}^{(2)} \mathbf{v}_1^{\delta 0}, \partial_\zeta \mathbf{v}_{1\parallel}^{d0} \right\rangle + \left\langle I_{q\zeta}^{(1)} \mathbf{v}_1^{\delta 0}, \partial_\zeta \mathbf{v}_{1\zeta}^{d0} \right\rangle \right\}. \tag{B8}
\end{aligned}$$

Splitting this into the parallel and perpendicular components $\mathbf{v}_{2\parallel}^{\delta v}$ and $\mathbf{v}_{2\zeta}^{\delta v}$, respectively, yields,

$$\begin{aligned}
\mathbf{v}_{2\parallel}^{\delta v} &= \frac{1}{\nu_0} \left\{ \nabla_{\parallel} \cdot \left\langle I_{qq}^{(2)} \mathbf{v}_{1\parallel}^{\delta 0}, \mathbf{v}_{1\parallel}^{\delta 0} \right\rangle + \left\langle I_{qq}^{(1)} \mathbf{v}_{1\parallel}^{\delta 0}, \mathbf{v}_{1\zeta}^{\delta 0} \right\rangle \right. \\
&\quad + \nabla_{\parallel} \cdot \left\langle I_{1q}^{(2)} \mathbf{v}_{1\parallel}^{d0}, \mathbf{v}_{1\parallel}^{\delta 0} \right\rangle + \left\langle I_{1q}^{(1)} \mathbf{v}_{1\parallel}^{d0}, \mathbf{v}_{1\zeta}^{\delta 0} \right\rangle \\
&\quad + \nabla_{\parallel} \cdot \left\langle I_{\zeta q}^{(2)} \partial_\zeta \mathbf{v}_{1\parallel}^{d0}, \mathbf{v}_{1\parallel}^{\delta 0} \right\rangle + \left\langle I_{\zeta q}^{(1)} \partial_\zeta \mathbf{v}_{1\parallel}^{d0}, \mathbf{v}_{1\zeta}^{\delta 0} \right\rangle \\
&\quad + \nabla_{\parallel} \cdot \left\langle I_{q1}^{(2)} \mathbf{v}_{1\parallel}^{\delta 0}, \mathbf{v}_{1\parallel}^{d0} \right\rangle + \left\langle I_{q1}^{(1)} \mathbf{v}_{1\parallel}^{\delta 0}, \mathbf{v}_{1\zeta}^{d0} \right\rangle \\
&\quad \left. + \nabla_{\parallel} \cdot \left\langle I_{q\zeta}^{(2)} \mathbf{v}_{1\parallel}^{\delta 0}, \partial_\zeta \mathbf{v}_{1\parallel}^{d0} \right\rangle + \left\langle I_{q\zeta}^{(1)} \mathbf{v}_{1\parallel}^{\delta 0}, \partial_\zeta \mathbf{v}_{1\zeta}^{d0} \right\rangle \right\} \tag{B9}
\end{aligned}$$

and

$$\begin{aligned}
\mathbf{v}_{2\zeta}^{\delta v} &= \frac{1}{\nu_0} \left\{ \nabla_{\parallel} \cdot \left\langle I_{qq}^{(2)} \mathbf{v}_{1\zeta}^{\delta 0}, \mathbf{v}_{1\parallel}^{\delta 0} \right\rangle + \left\langle I_{qq}^{(1)} \mathbf{v}_{1\zeta}^{\delta 0}, \mathbf{v}_{1\zeta}^{\delta 0} \right\rangle \right. \\
&\quad + \nabla_{\parallel} \cdot \left\langle I_{1q}^{(2)} \mathbf{v}_{1\zeta}^{d0}, \mathbf{v}_{1\parallel}^{\delta 0} \right\rangle + \left\langle I_{1q}^{(1)} \mathbf{v}_{1\zeta}^{d0}, \mathbf{v}_{1\zeta}^{\delta 0} \right\rangle \\
&\quad + \nabla_{\parallel} \cdot \left\langle I_{\zeta q}^{(2)} \partial_\zeta \mathbf{v}_{1\zeta}^{d0}, \mathbf{v}_{1\parallel}^{\delta 0} \right\rangle + \left\langle I_{\zeta q}^{(1)} \partial_\zeta \mathbf{v}_{1\zeta}^{d0}, \mathbf{v}_{1\zeta}^{\delta 0} \right\rangle \\
&\quad + \nabla_{\parallel} \cdot \left\langle I_{q1}^{(2)} \mathbf{v}_{1\zeta}^{\delta 0}, \mathbf{v}_{1\parallel}^{d0} \right\rangle + \left\langle I_{q1}^{(1)} \mathbf{v}_{1\zeta}^{\delta 0}, \mathbf{v}_{1\zeta}^{d0} \right\rangle \\
&\quad \left. + \nabla_{\parallel} \cdot \left\langle I_{q\zeta}^{(2)} \mathbf{v}_{1\zeta}^{\delta 0}, \partial_\zeta \mathbf{v}_{1\parallel}^{d0} \right\rangle + \left\langle I_{q\zeta}^{(1)} \mathbf{v}_{1\zeta}^{\delta 0}, \partial_\zeta \mathbf{v}_{1\zeta}^{d0} \right\rangle \right\}. \tag{B10}
\end{aligned}$$

Adding Eqs. (B6) and (B10), gives the full $\mathbf{v}_{2\zeta}^{\delta}$,

$$\begin{aligned}
\mathbf{v}_{2\zeta}^{\delta} &= \mathbf{v}_{2\zeta}^{\delta p} + \mathbf{v}_{2\zeta}^{\delta v} \\
&= -\frac{1}{\nu_0} \left\{ \right. \\
&\quad + \nabla_{\parallel} \cdot \left[\nabla_{\parallel} \cdot \left\langle I_{qq}^{(3)} \mathbf{v}_{1\parallel}^{\delta 0}, \mathbf{v}_{1\parallel}^{\delta 0} \right\rangle \right] + \nabla_{\parallel} \cdot \left\langle I_{qq}^{(2)} \mathbf{v}_{1\parallel}^{\delta 0}, \mathbf{v}_{1\zeta}^{\delta 0} \right\rangle \\
&\quad + \nabla_{\parallel} \cdot \left[\nabla_{\parallel} \cdot \left\langle I_{1q}^{(3)} \mathbf{v}_1^{d0}, \mathbf{v}_{1\parallel}^{\delta 0} \right\rangle \right] + \nabla_{\parallel} \cdot \left\langle I_{1q}^{(2)} \mathbf{v}_1^{d0}, \mathbf{v}_{1\zeta}^{\delta 0} \right\rangle \\
&\quad + \nabla_{\parallel} \cdot \left[\nabla_{\parallel} \cdot \left\langle I_{\zeta q}^{(3)} \partial_\zeta \mathbf{v}_1^{d0}, \mathbf{v}_{1\parallel}^{\delta 0} \right\rangle \right] + \nabla_{\parallel} \cdot \left\langle I_{\zeta q}^{(2)} \partial_\zeta \mathbf{v}_1^{d0}, \mathbf{v}_{1\zeta}^{\delta 0} \right\rangle \\
&\quad + \nabla_{\parallel} \cdot \left[\nabla_{\parallel} \cdot \left\langle I_{q1}^{(3)} \mathbf{v}_1^{\delta 0}, \mathbf{v}_{1\parallel}^{\delta 0} \right\rangle \right] + \nabla_{\parallel} \cdot \left\langle I_{q1}^{(2)} \mathbf{v}_1^{\delta 0}, \mathbf{v}_{1\zeta}^{\delta 0} \right\rangle \\
&\quad \left. + \nabla_{\parallel} \cdot \left[\nabla_{\parallel} \cdot \left\langle I_{q\zeta}^{(3)} \mathbf{v}_1^{\delta 0}, \partial_\zeta \mathbf{v}_{1\parallel}^{d0} \right\rangle \right] + \nabla_{\parallel} \cdot \left\langle I_{q\zeta}^{(2)} \mathbf{v}_1^{\delta 0}, \partial_\zeta \mathbf{v}_{1\zeta}^{d0} \right\rangle \right\}. \tag{B11}
\end{aligned}$$

4. The final expression for $\mathbf{v}_2^{\delta 0}$

Using the scalings $\frac{2}{\omega \delta^2} \hat{I}_{qq}^{(n)}$, $\frac{2}{\omega \delta^2} \hat{I}_{1q}^{(n)} \propto \delta^{n-2}$ and $\frac{2}{\omega \delta^2} \hat{I}_{\zeta q}^{(n)} \propto \delta^{n-1}$ obtained from Eq. (33), we neglect the terms of higher order in δ and obtain

$$\mathbf{v}_2^{\delta 0} = \mathbf{v}_{2\parallel}^{\delta 0} + \mathbf{v}_{2\zeta}^{\delta 0} \mathbf{e}_\zeta = \mathbf{v}_{2\parallel}^{\delta p 0} + \mathbf{v}_{2\parallel}^{\delta v 0} + \mathbf{v}_{2\zeta}^{\delta 0} \mathbf{e}_\zeta, \tag{B12a}$$

$$\begin{aligned}
\mathbf{v}_{2\parallel}^{\delta p 0} &= -\frac{2}{\omega \delta^2} \nabla_{\parallel} \left\{ \right. \\
&\quad + \nabla_{\parallel} \cdot \left[\nabla_{\parallel} \cdot \left\langle \hat{I}_{qq}^{(4)} \mathbf{v}_{1\parallel}^{\delta 0}, \mathbf{v}_{1\parallel}^{\delta 0} \right\rangle \right] + \left\langle \hat{I}_{qq}^{(2)} \mathbf{v}_{1\zeta}^{\delta 0}, \mathbf{v}_{1\zeta}^{\delta 0} \right\rangle \\
&\quad + \nabla_{\parallel} \cdot \left[\left\langle \hat{I}_{qq}^{(3)} \mathbf{v}_{1\parallel}^{\delta 0}, \mathbf{v}_{1\zeta}^{\delta 0} \right\rangle + \left\langle \hat{I}_{qq}^{(3)} \mathbf{v}_{1\zeta}^{\delta 0}, \mathbf{v}_{1\parallel}^{\delta 0} \right\rangle \right] \\
&\quad + \nabla_{\parallel} \cdot \left[\nabla_{\parallel} \cdot \left\langle \hat{I}_{1q}^{(4)} \mathbf{v}_1^{d0}, \mathbf{v}_{1\parallel}^{\delta 0} \right\rangle \right] + \left\langle \hat{I}_{1q}^{(2)} \mathbf{v}_1^{d0}, \mathbf{v}_{1\zeta}^{\delta 0} \right\rangle \\
&\quad + \nabla_{\parallel} \cdot \left[\left\langle \hat{I}_{1q}^{(3)} \mathbf{v}_1^{d0}, \mathbf{v}_{1\zeta}^{\delta 0} \right\rangle + \left\langle \hat{I}_{1q}^{(3)} \mathbf{v}_{1\zeta}^{d0}, \mathbf{v}_{1\parallel}^{\delta 0} \right\rangle \right] \\
&\quad + \nabla_{\parallel} \cdot \left[\nabla_{\parallel} \cdot \left\langle \hat{I}_{\zeta q}^{(4)} \partial_\zeta \mathbf{v}_1^{d0}, \mathbf{v}_{1\parallel}^{\delta 0} \right\rangle \right] + \left\langle \hat{I}_{\zeta q}^{(2)} \partial_\zeta \mathbf{v}_1^{d0}, \mathbf{v}_{1\zeta}^{\delta 0} \right\rangle \\
&\quad + \nabla_{\parallel} \cdot \left[\left\langle \hat{I}_{\zeta q}^{(3)} \partial_\zeta \mathbf{v}_1^{d0}, \mathbf{v}_{1\zeta}^{\delta 0} \right\rangle + \left\langle \hat{I}_{\zeta q}^{(3)} \partial_\zeta \mathbf{v}_{1\zeta}^{d0}, \mathbf{v}_{1\parallel}^{\delta 0} \right\rangle \right] \\
&\quad + \nabla_{\parallel} \cdot \left[\nabla_{\parallel} \cdot \left\langle \hat{I}_{q1}^{(4)} \mathbf{v}_1^{\delta 0}, \mathbf{v}_{1\parallel}^{\delta 0} \right\rangle \right] + \left\langle \hat{I}_{q1}^{(2)} \mathbf{v}_1^{\delta 0}, \mathbf{v}_{1\zeta}^{\delta 0} \right\rangle \\
&\quad + \nabla_{\parallel} \cdot \left[\left\langle \hat{I}_{q1}^{(3)} \mathbf{v}_1^{\delta 0}, \mathbf{v}_{1\zeta}^{\delta 0} \right\rangle + \left\langle \hat{I}_{q1}^{(3)} \mathbf{v}_{1\zeta}^{\delta 0}, \mathbf{v}_{1\parallel}^{\delta 0} \right\rangle \right] \\
&\quad + \nabla_{\parallel} \cdot \left[\nabla_{\parallel} \cdot \left\langle \hat{I}_{q\zeta}^{(4)} \mathbf{v}_1^{\delta 0}, \partial_\zeta \mathbf{v}_{1\parallel}^{d0} \right\rangle \right] + \left\langle \hat{I}_{q\zeta}^{(2)} \mathbf{v}_1^{\delta 0}, \partial_\zeta \mathbf{v}_{1\zeta}^{d0} \right\rangle \\
&\quad \left. + \nabla_{\parallel} \cdot \left[\left\langle \hat{I}_{q\zeta}^{(3)} \mathbf{v}_1^{\delta 0}, \partial_\zeta \mathbf{v}_{1\zeta}^{d0} \right\rangle + \left\langle \hat{I}_{q\zeta}^{(3)} \mathbf{v}_{1\zeta}^{\delta 0}, \partial_\zeta \mathbf{v}_{1\parallel}^{d0} \right\rangle \right] \right\}, \tag{B12b}
\end{aligned}$$

$$\begin{aligned}
\mathbf{v}_{2\parallel}^{\delta v0} = & \frac{2}{\omega\delta^2} \left\{ \nabla_{\parallel} \cdot \left\langle \hat{I}_{qq}^{(2)} \mathbf{v}_{1\parallel}^{\delta0}, \mathbf{v}_{1\parallel}^{\delta0} \right\rangle + \left\langle \hat{I}_{qq}^{(1)} \mathbf{v}_{1\parallel}^{\delta0}, v_{1\zeta}^{\delta0} \right\rangle \right. \\
& + \nabla_{\parallel} \cdot \left\langle \hat{I}_{1q}^{(2)} \mathbf{v}_{1\parallel}^{d0}, \mathbf{v}_{1\parallel}^{\delta0} \right\rangle + \left\langle \hat{I}_{1q}^{(1)} \mathbf{v}_{1\parallel}^{d0}, v_{1\zeta}^{\delta0} \right\rangle \\
& + \nabla_{\parallel} \cdot \left\langle \hat{I}_{\zeta q}^{(2)} \partial_{\zeta} \mathbf{v}_{1\parallel}^{d0}, \mathbf{v}_{1\parallel}^{\delta0} \right\rangle + \left\langle \hat{I}_{\zeta q}^{(1)} \partial_{\zeta} \mathbf{v}_{1\parallel}^{d0}, v_{1\zeta}^{\delta0} \right\rangle \\
& + \nabla_{\parallel} \cdot \left\langle \hat{I}_{q1}^{(2)} \mathbf{v}_{1\parallel}^{\delta0}, \mathbf{v}_{1\parallel}^{d0} \right\rangle + \left\langle \hat{I}_{q1}^{(1)} \mathbf{v}_{1\parallel}^{\delta0}, v_{1\zeta}^{d0} \right\rangle \\
& \left. + \nabla_{\parallel} \cdot \left\langle \hat{I}_{q\zeta}^{(2)} \mathbf{v}_{1\parallel}^{\delta0}, \partial_{\zeta} \mathbf{v}_{1\parallel}^{d0} \right\rangle + \left\langle \hat{I}_{q\zeta}^{(1)} \mathbf{v}_{1\parallel}^{\delta0}, \partial_{\zeta} v_{1\zeta}^{d0} \right\rangle \right\}, \quad (\text{B12c})
\end{aligned}$$

$$\begin{aligned}
\mathbf{v}_{2\parallel}^{\delta0} = & \frac{2}{\omega\delta^2} \left\{ -\nabla_{\parallel} \left[\left\langle \hat{I}_{qq}^{(2)} \mathbf{v}_{1\zeta}^{\delta0}, \mathbf{v}_{1\zeta}^{\delta0} \right\rangle \right. \right. \\
& + \left\langle \hat{I}_{1q}^{(2)} v_{1\zeta}^{d0}, v_{1\zeta}^{\delta0} \right\rangle + \left\langle \hat{I}_{q1}^{(2)} v_{1\zeta}^{\delta0}, v_{1\zeta}^{d0} \right\rangle \\
& + \nabla_{\parallel} \cdot \left\langle \hat{I}_{qq}^{(2)} \mathbf{v}_{1\parallel}^{\delta0}, \mathbf{v}_{1\parallel}^{\delta0} \right\rangle + \left\langle \hat{I}_{qq}^{(1)} \mathbf{v}_{1\parallel}^{\delta0}, v_{1\zeta}^{\delta0} \right\rangle \\
& + \nabla_{\parallel} \cdot \left\langle \hat{I}_{1q}^{(2)} \mathbf{v}_{1\parallel}^{d0}, \mathbf{v}_{1\parallel}^{\delta0} \right\rangle + \left\langle \hat{I}_{1q}^{(1)} \mathbf{v}_{1\parallel}^{d0}, v_{1\zeta}^{\delta0} \right\rangle \\
& + \nabla_{\parallel} \cdot \left\langle \hat{I}_{q1}^{(2)} \mathbf{v}_{1\parallel}^{\delta0}, \mathbf{v}_{1\parallel}^{d0} \right\rangle + \left\langle \hat{I}_{q1}^{(1)} \mathbf{v}_{1\parallel}^{\delta0}, v_{1\zeta}^{d0} \right\rangle \\
& \left. + \left\langle \hat{I}_{\zeta q}^{(1)} \partial_{\zeta} \mathbf{v}_{1\parallel}^{d0}, v_{1\zeta}^{\delta0} \right\rangle + \left\langle \hat{I}_{q\zeta}^{(1)} \mathbf{v}_{1\parallel}^{\delta0}, \partial_{\zeta} v_{1\zeta}^{d0} \right\rangle \right\}, \quad (\text{B12d})
\end{aligned}$$

and

$$\begin{aligned}
v_{2\zeta}^{\delta0} = & v_{2\zeta}^{\delta p0} + v_{2\zeta}^{\delta v0} \\
= & -\frac{2}{\omega\delta^2} \left\{ +\nabla_{\parallel} \cdot \left[\nabla_{\parallel} \cdot \left\langle \hat{I}_{qq}^{(3)} \mathbf{v}_{1\parallel}^{\delta0}, \mathbf{v}_{1\parallel}^{\delta0} \right\rangle + \left\langle \hat{I}_{qq}^{(2)} \mathbf{v}_{1\parallel}^{\delta0}, v_{1\zeta}^{\delta0} \right\rangle \right] \right. \\
& + \nabla_{\parallel} \cdot \left[\nabla_{\parallel} \cdot \left\langle \hat{I}_{1q}^{(3)} \mathbf{v}_{1\parallel}^{d0}, \mathbf{v}_{1\parallel}^{\delta0} \right\rangle + \left\langle \hat{I}_{1q}^{(2)} \mathbf{v}_{1\parallel}^{d0}, v_{1\zeta}^{\delta0} \right\rangle \right] \\
& + \nabla_{\parallel} \cdot \left[\nabla_{\parallel} \cdot \left\langle \hat{I}_{\zeta q}^{(3)} \partial_{\zeta} \mathbf{v}_{1\parallel}^{d0}, \mathbf{v}_{1\parallel}^{\delta0} \right\rangle + \left\langle \hat{I}_{\zeta q}^{(2)} \partial_{\zeta} \mathbf{v}_{1\parallel}^{d0}, v_{1\zeta}^{\delta0} \right\rangle \right] \\
& + \nabla_{\parallel} \cdot \left[\nabla_{\parallel} \cdot \left\langle \hat{I}_{q1}^{(3)} \mathbf{v}_{1\parallel}^{\delta0}, \mathbf{v}_{1\parallel}^{d0} \right\rangle + \left\langle \hat{I}_{q1}^{(2)} \mathbf{v}_{1\parallel}^{\delta0}, v_{1\zeta}^{d0} \right\rangle \right] \\
& \left. + \nabla_{\parallel} \cdot \left[\nabla_{\parallel} \cdot \left\langle \hat{I}_{q\zeta}^{(3)} \mathbf{v}_{1\parallel}^{\delta0}, \partial_{\zeta} \mathbf{v}_{1\parallel}^{d0} \right\rangle + \left\langle \hat{I}_{q\zeta}^{(2)} \mathbf{v}_{1\parallel}^{\delta0}, \partial_{\zeta} v_{1\zeta}^{d0} \right\rangle \right] \right\}. \quad (\text{B12e})
\end{aligned}$$

APPENDIX C: IMPLEMENTATION IN COMSOL OF THE SECOND-ORDER BOUNDARY CONDITION

The basic COMSOL Multiphysics syntax for implementing the BL25 model is presented in Sec. VI together with the COMSOL implementation (written in the “tt-typeface”) of the BL25 fluid-solid first-order boundary conditions. To implement the more involved second-order BL25 slip-velocity boundary condition, Eq. (39), we need to provide COMSOL implementations for terms of the following forms: (A) $\nabla_{\parallel} \left\langle \hat{I}_{qq}^{(2)} \mathbf{v}_{1\zeta}^{\delta0}, \mathbf{v}_{1\zeta}^{\delta0} \right\rangle$, (B) $\nabla_{\parallel} \cdot \left\langle \hat{I}_{qq}^{(2)} \mathbf{v}_{1\parallel}^{\delta0}, \mathbf{v}_{1\parallel}^{\delta0} \right\rangle$, and (C) $\left\langle \hat{I}_{q\zeta}^{(1)} \mathbf{v}_{1\parallel}^{\delta0}, \partial_{\zeta} v_{1\zeta}^{d0} \right\rangle$ from Eq. (35b);

(D) $\nabla_{\parallel} \cdot \nabla_{\parallel} \cdot \left\langle \hat{I}_{qq}^{(3)} \mathbf{v}_{1\parallel}^{\delta0}, \mathbf{v}_{1\parallel}^{\delta0} \right\rangle$ and (E) $\nabla_{\parallel} \cdot \left\langle \hat{I}_{q1}^{(2)} \mathbf{v}_{1\parallel}^{\delta0}, v_{1\zeta}^{d0} \right\rangle$ from Eq. (35c); and (F) $\left\langle i\mathbf{V}_1^0 \cdot \nabla \mathbf{v}_1^{d0} + \nabla_{\parallel} \mathbf{v}_1^{\delta0} \right\rangle + \left\langle V_{1\zeta}^0, k_{\zeta} \mathbf{v}_1^{\delta0} \right\rangle$ from Eq. (38).

In the following, we implement (A)-(F) term by term. However, we note that in expressions containing a parallel vector $\mathbf{v}_{1\parallel}^{\delta0}$, it is easier to implement the full vector $\mathbf{v}_1^{\delta0}$, and then project the final result onto the tangential plane spanned by the tangent vector \mathbf{t}_1 and \mathbf{t}_2 . The procedure is exemplified as follows:

$$\nabla_{\parallel} \cdot \left\langle \hat{I}_{qq}^{(2)} \mathbf{v}_{1\parallel}^{\delta0}, \mathbf{v}_{1\parallel}^{\delta0} \right\rangle = (\mathbf{W} \cdot \mathbf{t}_1) \mathbf{t}_1 + (\mathbf{W} \cdot \mathbf{t}_2) \mathbf{t}_2, \quad (\text{C1a})$$

$$\text{for } \mathbf{W} = \nabla_{\parallel} \cdot \left\langle \hat{I}_{qq}^{(2)} \mathbf{v}_1^{\delta0}, \mathbf{v}_1^{\delta0} \right\rangle. \quad (\text{C1b})$$

In each term, the tangential derivative ∇_{\parallel} projects one of the velocity fields onto the tangential plane, but not the other. Hence the necessity of the final tangent-plane projection. In COMSOL, the K th component of the tangent-plane projection of \mathbf{W} is given by the expression “(WX*t1X+WY*t1Y+WZ*t1Z)*t1K+(WX*t2X+WY*t2Y+WZ*t2Z)*t2K”.

(A) Introducing the tangential divergence “divparvd10 = vd1XtX+vd1YtY+vd1ZtZ”, $v_{1\zeta}^{\delta0}$ is given by Eq. (20) as “vd1zeta = (i/ks)*divparvd10”. Next, with “twoOVERomgdsqr” being the prefactor $\frac{2}{\omega\delta^2}$, all factors $\hat{I}_{ab}^{(n)}$ of Eq. (33) multiplied by $\frac{2}{\omega\delta^2}$ are called “Jabn”, e.g., “Jqz2 = twoOVERomgdsqr*(-(1-i)/2)*dvisc^3”. With “Jqq2vd1zetavd1zeta = 1/2*realdot(Jqq2*vd1zeta,vd1zeta)”, the k th component of the tangential gradient $\frac{2}{\omega\delta^2} \nabla_{\parallel} \left\langle \hat{I}_{qq}^{(2)} \mathbf{v}_{1\zeta}^{\delta0}, v_{1\zeta}^{\delta0} \right\rangle$ is implemented as “dtang(Jqq2vd1zetavd1zeta,k)” followed by the tangent-plane projection (C1).

(B) Since $\nabla_{\parallel} \cdot \left\langle \hat{I}_{qq}^{(2)} \mathbf{v}_{1\parallel}^{\delta0}, \mathbf{v}_{1\parallel}^{\delta0} \right\rangle = \left\langle \hat{I}_{qq}^{(2)} \mathbf{v}_{1\parallel}^{\delta0}, \nabla_{\parallel} \cdot \mathbf{v}_{1\parallel}^{\delta0} \right\rangle + \left\langle \hat{I}_{qq}^{(2)} \nabla_{\parallel} \mathbf{v}_{1\parallel}^{\delta0}, \mathbf{v}_{1\parallel}^{\delta0} \right\rangle$, we introduce for $K = X, Y,$ and Z the intermediate variable “Jqq2vd1KDIVvd10 = 0.5*realdot(Jqq2*vd1K,divparvd10)” together with “Jqq2DOTGRADvd1Kvd10 = 0.5*realdot(Jqq2*vd1KtX,vd1X)+0.5*realdot(Jqq2*vd1KtY,vd1Y)+0.5*realdot(Jqq2*vd1KtZ,vd1Z)”. Consequently, the K th component of $\frac{2}{\omega\delta^2} \nabla_{\parallel} \cdot \left\langle \hat{I}_{qq}^{(2)} \mathbf{v}_{1\parallel}^{\delta0}, \mathbf{v}_{1\parallel}^{\delta0} \right\rangle$ is implemented as “Jqq2vd1KDIVvd10+Jqq2DOTGRADvd1Kvd10” followed by the tangent-plane projection (C1).

(C) Using Eq. (15a) and the tangential divergence, we find $\partial_{\zeta} v_{1\zeta}^{d0} = \nabla \cdot \mathbf{v}_1^{d0} - \nabla_{\parallel} \cdot \mathbf{v}_1^{d0} = i\omega\kappa_0 p_1^0 - \nabla_{\parallel} \cdot \mathbf{v}_1^{d0}$, and therefore we introduce the variables “divparvf10 = vf1XtX+vf1YtY+vf1ZtZ” and “vf1zetazeta = i*kap0*omega*p1-divparvf10”. The K th component of $\frac{2}{\omega\delta^2} \left\langle \hat{I}_{q\zeta}^{(1)} \mathbf{v}_{1\parallel}^{\delta0}, \partial_{\zeta} v_{1\zeta}^{d0} \right\rangle$ is then simply implemented as

“0.5*realdot(Jqz1*vd1K,vf1zetazeta)”, followed by the tangent-plane projection (C1).

(D) We have $\nabla_{\parallel} \cdot \nabla_{\parallel} \cdot \langle \hat{\Gamma}_{qq}^{(3)} \mathbf{v}_{1\parallel}^{\delta 0}, \mathbf{v}_{1\parallel}^{\delta 0} \rangle = \nabla_{\parallel} \cdot \nabla_{\parallel} \cdot \langle \hat{\Gamma}_{qq}^{(3)} \mathbf{v}_{1\parallel}^{\delta 0}, \mathbf{v}_{1\parallel}^{\delta 0} \rangle$, since the two tangential divergences ensure that the full 3D vectors are projected onto the tangent plane. Now, the K th component of the vector resulting after the first ∇_{\parallel} is “DIVJqq3vd1Kvd1 = 0.5*(dtang(realdot(Jqq3*vd1K, vd1X), x) + dtang(realdot(Jqq3*vd1K, vd1Y), y) + dtang(realdot(Jqq3*vd1K, vd1Z), z))”. So $\frac{2}{\omega \delta^2} \nabla_{\parallel} \cdot \langle \hat{\Gamma}_{qq}^{(3)} \mathbf{v}_{1\parallel}^{\delta 0}, \mathbf{v}_{1\parallel}^{\delta 0} \rangle$ is simply implemented as “dtang(DIVJqq3vd1Xvd1, x) + dtang(DIVJqq3vd1Yvd1, y) + dtang(DIVJqq3vd1Zvd1, z)”.

(E) We have $\nabla_{\parallel} \cdot \langle \hat{\Gamma}_{q1}^{(2)} \mathbf{v}_{1\parallel}^{\delta 0}, v_{1\zeta}^{d0} \rangle = \nabla_{\parallel} \cdot \langle \hat{\Gamma}_{q1}^{(2)} \mathbf{v}_{1\parallel}^{\delta 0}, v_{1\zeta}^{d0} \rangle$, since the tangential divergence ensures that $\mathbf{v}_{1\parallel}^{\delta 0}$ is projected onto the tangent plane. The K th component of the argument to the divergence is implemented as “Jq12vd1Kvf1zeta = 0.5*realdot(Jq12*vd1X, vf1zeta)”, and therefore $\frac{2}{\omega \delta^2} \nabla_{\parallel} \cdot \langle \hat{\Gamma}_{q1}^{(2)} \mathbf{v}_{1\parallel}^{\delta 0}, v_{1\zeta}^{d0} \rangle$ is implemented simply as “dtang(Jq12vd1Xvf1zeta, x) + dtang(Jq12vd1Yvf1zeta, y) + dtang(Jq12vd1Zvf1zeta, z)”.

(F) The Stokes-drift contribution is the term $(1/\omega) [\langle i\mathbf{V}_1^0, \nabla \mathbf{v}_1^{d0} + \nabla_{\parallel} \mathbf{v}_1^{\delta 0} \rangle + \langle V_{1\zeta}^0, k_s \mathbf{v}_1^{\delta 0} \rangle]$. Its K th component is implemented as “vSD2K = 0.5/omega*(realdot(i*vs1X, vf1KX+vd1XtX) + realdot(i*vs1Y, vf1KY+vd1XtY) + realdot(i*vs1Z, vf1KZ+vd1XtZ) + realdot(vs1zeta, ks*vd1K))”. The perpendicular component is given by “vSD2zeta = nX*vSD2X + nY*vSD2Y + nZ*vSD2Z0” and the K th component of the tangential projection is “vSD2parK = vSD2K - nK*vSD2zeta”.

The final BL25 model slip velocity boundary condition (39) is obtained by adding all terms of the six basic forms (A)-(F). One form may have several contributions with different pre-factors “Jabn”, $a, b = 1, q, \zeta$ and $n = 1, 2, 3$, and different velocity components. For completeness, a COMSOL script of the BL25 model in 2D is provided in the Supplemental Material [37] together with some additional comments.

APPENDIX D: MESH-CONVERGENCE STUDY

We have performed a standard mesh-convergence study [22]. In 2D simulations, the solid PMMA, glue layer, and PZT domains are discretized using a free triangular mesh with maximum and minimum element sizes $h_{\max}^{\text{sl}} =$

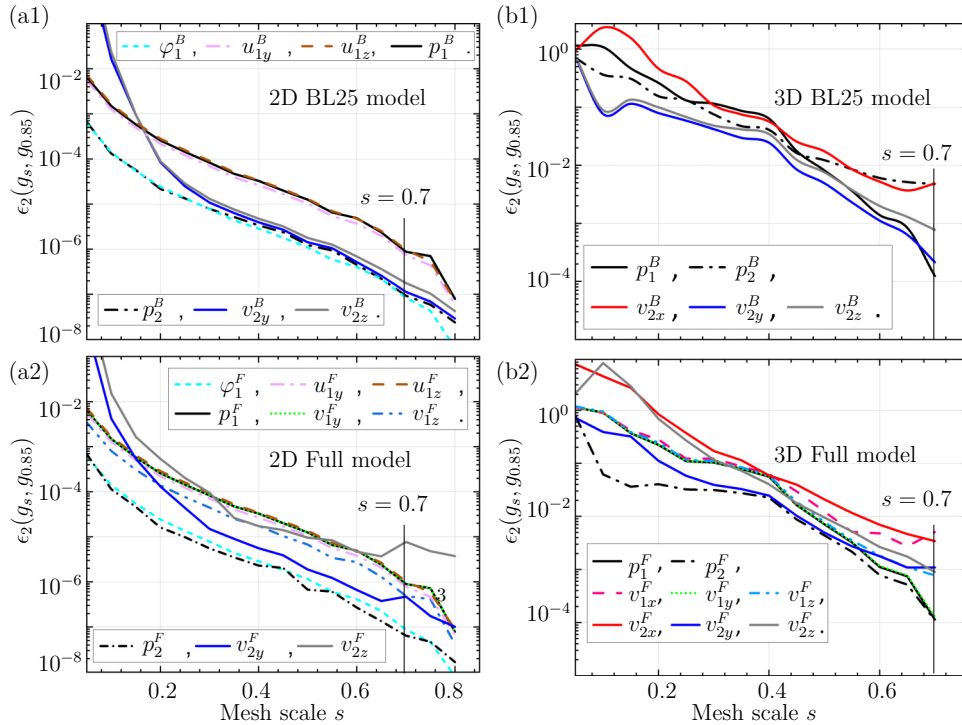


FIG. 5. Semilogarithmic mesh-convergence plot of the relative deviation $\epsilon_2(g_s, g_{0.85})$ defined in Eq. (43) versus the scaling parameter s . (a1) BL25 model in 2D: field components in first order $\varphi_1^B, u_{1y}^B, u_{1z}^B$, and p_1^B , and in second order p_2^B, v_{2y}^B , and v_{2z}^B . (a2) Full model in 2D: field components in first order $\varphi_1^F, u_{1y}^F, u_{1z}^F, p_1^F, v_{1y}^F$, and v_{1z}^F , and in second order p_2^F, v_{2y}^F , and v_{2z}^F . (b1) BL25 model in 3D: field components in first order p_1^B , and in second order $p_2^B, v_{2x}^B, v_{2y}^B$, and v_{2z}^B . (b2) Full model in 3D: field components in first order p_1^F, v_{1x}^F , and v_{1y}^F , and in second order $v_{1z}^F, p_2^F, v_{2x}^F, v_{2y}^F$, and v_{2z}^F .

$0.4H_f/s$ and $h_{\min}^{\text{sl}} = 0.025h_{\max}^{\text{sl}}$, where s is the scaling parameter that is gradually increased for refining the mesh. Since the electrode thickness is small, we have used the COMSOL mapped mesh with 40 as the number of elements for smoothing the mesh from the glue layer to the PZT. For the fluid domain, we defined maximum and minimum element sizes as $h_{\max}^{\text{fl}} = h_{\min}^{\text{sl}}$ and $h_{\min}^{\text{fl}} = 0.12h_{\max}^{\text{fl}}$. Further, we have used the boundary-layer mesh to accurately capture velocity fields in the Full model. The boundary-layer field is defined across the fluid-solid interface using eight layers, with the first layer of 0.2δ and a stretching factor of 1.2 so that we have in total a depth of 3.4δ .

In the case of the Full model in 3D, the solid PMMA domain is discretized using the free triangular mesh with maximum and minimum element sizes $h_{\max}^{\text{sl}} = 0.7H_f/s$ and $h_{\min}^{\text{sl}} = 0.125h_{\max}^{\text{sl}}$. Since the thin-film transducer is of thickness of $2\ \mu\text{m}$, we discretized the transducer using the structured swept mesh with the sweep directed from the top surface of the thin-film transducer. We discretized the fluid domain with a triangular mesh of maximum and minimum element sizes $h_{\max}^{\text{fl}} = h_{\min}^{\text{sl}}$ and $h_{\min}^{\text{fl}} = 0.6h_{\max}^{\text{fl}}$. Since a much finer mesh is required at the fluid-solid interface for the Full model to converge, we have used an edge mesh at the interface with maximum element size $h_{\max}^{\text{edge}} = 0.45h_{\max}^{\text{fl}}$. Further, we have implemented the boundary-layer mesh using eight layers to resolve the boundary-layer fields with the first-layer thickness set to 0.2δ .

For the BL25 model in 3D, we use a much coarser mesh inside the fluid domain and we do not need a boundary-layer mesh. Accordingly, the solid PMMA domain is discretized using the triangular mesh with maximum and minimum element sizes $h_{\max}^{\text{sl}} = 0.4H_f/s$ and $h_{\min}^{\text{sl}} = 0.2h_{\max}^{\text{sl}}$. Similar to the 3D Full model, we use a swept mesh for the thin-film transducer, and coarser triangular mesh in the fluid domain with maximum and minimum element sizes $h_{\max}^{\text{fl}} = h_{\min}^{\text{sl}}$ and $h_{\min}^{\text{fl}} = 0.6h_{\max}^{\text{fl}}$. In Fig. 5, the relative deviation $\epsilon_2(g_s, g_{0.85})$, defined in Eq. (43), of the solution g_s with mesh scale s from the solution $g_{0.85}$ with the maximum mesh scale $s = 0.85$ (the finest mesh) is plotted in a semilogarithmic plot versus the mesh scale s for both the 2D and the 3D simulation models.

[1] T. Laurell and A. Lenshof (eds.), *Microscale Acoustofluidics* (Royal Society of Chemistry, Cambridge, 2015).
 [2] Y. Fan, X. Wang, J. Ren, F. Lin, and J. Wu, Recent advances in acoustofluidic separation technology in biology, *Microsyst. Nanoeng.* **8**, 94 (2022).
 [3] D. Van Assche, E. Reithuber, W. Qiu, T. Laurell, B. Henriques-Normark, P. Mellroth, P. Ohlsson, and P. Augustsson, Gradient acoustic focusing of sub-micron particles for separation of bacteria from blood lysate, *Sci. Rep.* **10**, 3670 (2020).

[4] E. U. Anand, C. Magnusson, A. Lenshof, Y. Ceder, H. Lilja, and T. Laurell, Two-step acoustophoresis separation of live tumor cells from whole blood, *Anal. Chem.* **93**, 17076 (2021).
 [5] M. Anwar, N. M. Reis, C. Zhang, A. Khan, K. A. Kalhor, A. U. Rehman, Y. Zhang, and Z. Liu, Microfluidic devices for the isolation and label-free identification of circulating tumor cells, *J. Chem. Eng.* **499**, 156497 (2024).
 [6] W. Qiu, T. Baasch, and T. Laurell, Enhancement of acoustic energy density in bulk-wave-acoustophoresis devices using side actuation, *Phys. Rev. Appl.* **17**, 044043 (2022).
 [7] T. Baasch, W. Qiu, and T. Laurell, Whole-channel acoustic energy and acoustophoretic efficiency frequency spectrum by the in-flow focusing method, *Phys. Rev. Appl.* **22**, 044049 (2024).
 [8] M. Wu, A. Ozcelik, J. Rufo, Z. Wang, R. Fang, and T. J. Huang, Acoustofluidic separation of cells and particles, *Microsyst. Nanoeng.* **5**, 32 (2019).
 [9] E. Hemachandran, S. Z. Hoque, T. Laurell, and A. K. Sen, Reversible stream drop transition in a microfluidic coflow system via on demand exposure to acoustic standing waves, *Phys. Rev. Lett.* **127**, 134501 (2021).
 [10] S. Z. Hoque and A. K. Sen, Dynamics of a two-layer immiscible fluid system exposed to ultrasound, *J. Acoust. Soc. Am.* **155**, 1655 (2024).
 [11] S. Deshmukh, Z. Brzozka, T. Laurell, and P. Augustsson, Acoustic radiation forces at liquid interfaces impact the performance of acoustophoresis, *Lab Chip* **14**, 3394 (2014).
 [12] J. T. Karlsen, P. Augustsson, and H. Bruus, Acoustic force density acting on inhomogeneous fluids in acoustic fields, *Phys. Rev. Lett.* **117**, 114504 (2016).
 [13] P. Augustsson, J. T. Karlsen, H.-W. Su, H. Bruus, and J. Voldman, Iso-acoustic focusing of cells for size-insensitive acousto-mechanical phenotyping, *Nat. Commun.* **7**, 11556 (2016).
 [14] J. T. Karlsen, W. Qiu, P. Augustsson, and H. Bruus, Acoustic streaming and its suppression in inhomogeneous fluids, *Phys. Rev. Lett.* **120**, 054501 (2018).
 [15] A. Lenshof, M. Evander, T. Laurell, and J. Nilsson, Acoustofluidics 5: Building microfluidic acoustic resonators, *Lab Chip* **12**, 684 (2012).
 [16] W. J. Savage, J. R. Burns, and J. Fiering, Safety of acoustic separation in plastic devices for extracorporeal blood processing, *Transfusion* **57**, 1818 (2017).
 [17] C. Yang, Z. Li, P. Li, W. Shao, P. Bai, and Y. Cui, Acoustic particle sorting by integrated micromachined ultrasound transducers on polymer-based microchips, in *IEEE International Ultrasonics Symposium (IUS)*, p. 1 (Curran Associates, Inc., Reed Hook (NY) USA, 2017).
 [18] R. Silva, P. Dow, R. Dubay, C. Lissandrello, J. Holder, D. Densmore, and J. Fiering, Rapid prototyping and parametric optimization of plastic acoustofluidic devices for blood-bacteria separation, *Biomed. Microdevices* **19**, 70 (2017).
 [19] R. Dubay, C. Lissandrello, P. Swierk, N. Moore, D. Doty, and J. Fiering, Scalable high-throughput acoustophoresis in arrayed plastic microchannels, *Biomicrofluidics* **13**, 034105 (2019).

- [20] F. Lickert, M. Ohlin, H. Bruus, and P. Ohlsson, Acoustophoresis in polymer-based microfluidic devices: Modeling and experimental validation, *J. Acoust. Soc. Am.* **149**, 4281 (2021).
- [21] R. P. Moiseyenko and H. Bruus, Whole-system ultrasound resonances as the basis for acoustophoresis in all-polymer microfluidic devices, *Phys. Rev. Appl.* **11**, 014014 (2019).
- [22] P. B. Muller, R. Barnkob, M. J. H. Jensen, and H. Bruus, A numerical study of microparticle acoustophoresis driven by acoustic radiation forces and streaming-induced drag forces, *Lab Chip* **12**, 4617 (2012).
- [23] P. B. Muller, M. Rossi, A. G. Marin, R. Barnkob, P. Augustsson, T. Laurell, C. J. Kähler, and H. Bruus, Ultrasound-induced acoustophoretic motion of microparticles in three dimensions, *Phys. Rev. E* **88**, 023006 (2013).
- [24] P. B. Muller and H. Bruus, Numerical study of thermoviscous effects in ultrasound-induced acoustic streaming in microchannels, *Phys. Rev. E* **90**, 043016 (2014).
- [25] P. Hahn and J. Dual, A numerically efficient damping model for acoustic resonances in microfluidic cavities, *Phys. Fluids* **27**, 062005 (2015).
- [26] M. W. H. Ley and H. Bruus, Continuum modeling of hydrodynamic particle-particle interactions in microfluidic high-concentration suspensions, *Lab Chip* **16**, 1178 (2016).
- [27] B. Hammarström, T. Laurell, and J. Nilsson, Seed particle enabled acoustic trapping of bacteria and nanoparticles in continuous flow systems, *Lab Chip* **12**, 4296 (2012).
- [28] M. Antfolk, C. Magnusson, P. Augustsson, H. Lilja, and T. Laurell, Acoustofluidic, label-free separation and simultaneous concentration of rare tumor cells from white blood cells, *Anal. Chem.* **87**, 9322 (2015).
- [29] Z. Mao, P. Li, M. Wu, H. Bachman, N. Mesyngier, X. Guo, S. Liu, F. Costanzo, and T. J. Huang, Enriching nanoparticles via acoustofluidics, *ACS Nano* **11**, 603 (2017).
- [30] D. J. Collins, Z. Ma, J. Han, and Y. Ai, Continuous microvortex-based nanoparticle manipulation via focused surface acoustic waves, *Lab Chip* **17**, 91 (2017).
- [31] J. S. Bach and H. Bruus, Theory of pressure acoustics with viscous boundary layers and streaming in curved elastic cavities, *J. Acoust. Soc. Am.* **144**, 766 (2018).
- [32] W. L. Nyborg, Acoustic streaming near a boundary, *J. Acoust. Soc. Am.* **30**, 329 (1958).
- [33] C. Lee and T. Wang, Near-boundary streaming around a small sphere due to two orthogonal standing waves, *J. Acoust. Soc. Am.* **85**, 1081 (1989).
- [34] J. Vanneste and O. Bühler, Streaming by leaky surface acoustic waves, *Proc. R. Soc. A* **467**, 1779 (2011).
- [35] N. R. Skov, J. S. Bach, B. G. Winkelmann, and H. Bruus, 3D modeling of acoustofluidics in a liquid-filled cavity including streaming, viscous boundary layers, surrounding solids, and a piezoelectric transducer, *AIMS Math.* **4**, 99 (2019).
- [36] S. M. Hagsäter, T. G. Jensen, H. Bruus, and J. P. Kutter, Acoustic resonances in microfluidic chips: Full-image micro-PIV experiments and numerical simulations, *Lab Chip* **7**, 1336 (2007).
- [37] See Supplemental Material at <http://link.aps.org/supplemental/10.1103/m1rf-tpkw> for an analysis of corner effects in 2D and 3D rectangular channels, for details on the dependence on the glue-layer thickness, and for a COMSOL sample script.
- [38] *Glass Silicon Constraint Substrates*, CORNING, Houghton Park C-8, Corning, NY 14831, USA, <http://www.valleydesign.com/Datasheets/Corning%20Pyrex%207740.pdf> (accessed 30 September 2025).
- [39] W. N. Bodé, F. Lickert, P. Augustsson, and H. Bruus, Determination of the complex-valued elastic moduli of polymers by electrical-impedance spectroscopy for ultrasound applications, *Phys. Rev. Appl.* **18**, 064078 (2022).
- [40] A. G. Steckel, H. Bruus, P. Muralt, and R. Matloub, Fabrication, characterization, and simulation of glass devices with AlN thin-film transducers for excitation of ultrasound resonances, *Phys. Rev. Appl.* **16**, 014014 (2021).
- [41] A. G. Steckel and H. Bruus, Numerical study of bulk acoustofluidic devices driven by thin-film transducers and whole-system resonance modes, *J. Acoust. Soc. Am.* **150**, 634 (2021).
- [42] COMSOL Multiphysics 6.2, COMSOL, <http://www.comsol.com> (2023).
- [43] J. H. Joergensen and H. Bruus, Theory and modeling of nonperturbative effects in thermoviscous acoustofluidics, *Phys. Rev. E* **107**, 015106 (2023).
- [44] N.-S. Cheng, Formula for the viscosity of a glycerol-water mixture, *Ind. Eng. Chem. Res.* **47**, 3285 (2008).
- [45] W. N. Bodé, L. Jiang, T. Laurell, and H. Bruus, Microparticle acoustophoresis in aluminum-based acoustofluidic devices with PDMS covers, *Micromachines* **11**, 292 (2020).
- [46] M. A. Caro, S. Zhang, T. Riekkinen, M. Ylilampi, M. A. Moram, O. Lopez-Acevedo, J. Molarius, and T. Laurila, Piezoelectric coefficients and spontaneous polarization of ScAlN, *J. Phys.-Condens. Matter* **27**, 245901 (2015).
- [47] R. H. Olsson, Z. Tang, and M. D'Agati, Doping of aluminum nitride and the impact on thin film piezoelectric and ferroelectric device performance, in *2020 IEEE Custom Integrated Circuits Conference (CICC)* (Curran Associates, Inc., Reed Hook (NY) USA, 2020), p. 1.
- [48] M. Antfolk, P. B. Muller, P. Augustsson, H. Bruus, and T. Laurell, Focusing of sub-micrometer particles and bacteria enabled by two-dimensional acoustophoresis, *Lab Chip* **14**, 2791 (2014).
- [49] Pz27 soft PZT, CTS|Ferropem, Porthusvej 4, DK-3490 Kvistgaard, Denmark (2025), <https://www.ctscorp.com/Product-Series/Pz27.htm> (accessed 30 September 2025).
- [50] J. S. Bach and H. Bruus, Bulk-driven acoustic streaming at resonance in closed microcavities, *Phys. Rev. E* **100**, 023104 (2019).
- [51] J. S. Bach and H. Bruus, Suppression of acoustic streaming in shape-optimized channels, *Phys. Rev. Lett.* **124**, 214501 (2020).
- [52] S. Li, W. Cui, T. Baasch, B. Wang, and Z. Gong, Eckart streaming with nonlinear high-order harmonics: An example at gigahertz, *Phys. Rev. Fluids* **9**, 084201 (2024).
- [53] J. H. Joergensen, W. Qiu, and H. Bruus, Transition from boundary-driven to bulk-driven acoustic streaming due to nonlinear thermoviscous effects at high acoustic energy densities, *Phys. Rev. Lett.* **130**, 044001 (2023).
- [54] Pz26 hard PZT, CTS|Ferropem, Porthusvej 4, DK-3490 Kvistgaard, Denmark (2025), <https://www.ctscorp.com/Product-Series/Pz26.htm> (accessed 30 September 2025).